

An accurate machine learning interatomic potential for FCC and HCP nickel

Xiaoguo Gong, Zhuoyuan Li, A. S. L. Subrahmanyam Pattamatta, Tongqi Wen,^{*} and David J. Srolovitz[†]
Department of Mechanical Engineering, The University of Hong Kong, Hong Kong Special Administrative Region of China

Nickel (Ni) is a commonly used metal and critical component in various structural alloys such as superalloys. It exhibits two allotropy phases, namely stable face-centered cubic (FCC) and metastable hexagonal close-packed (HCP) phases. Recent studies, both experimental and computational, have focused on the phase transformation and defect properties in allotropic Ni. However, accurate density functional theory (DFT) calculations are computationally inefficient and insufficient for studying the material behavior which often necessitates the system size exceeding one thousand atoms and simulation time surpassing one nanosecond. In this study, we implement a straightforward strategy to deal with atomic spin polarization in Ni for developing a machine-learning Deep Potential (DP) model for Ni FCC and HCP phases, using training datasets derived from spin-polarized DFT calculations. The resulting DP-Ni model demonstrates high transferability and representability across various properties among allotropies, such as (finite-temperature) lattice parameters, elastic constants, phonon spectra, and defect properties. The examination of the FCC-HCP allotropic transition under uniaxial tensile conditions unveiled a substantial critical strain requirement, in which the orientation relationship is $\{100\}_{\text{FCC}} \parallel \{0001\}_{\text{HCP}}$ and $\langle 010 \rangle_{\text{FCC}} \parallel \langle 11\bar{2}0 \rangle_{\text{HCP}}$. The DP-Ni model not only facilitates accurate large-scale atomistic simulations for complex mechanical behaviors, but also serves as a foundation for developing interatomic potentials for Ni-based superalloys and other multi-principal component alloys.

I. INTRODUCTION

Nickel, with its high melting point, density, ductility, and strength, as well as exceptional corrosion and oxidation resistance [1, 2], is vital for numerous industrial applications. It is widely employed in turbine blades, aircraft engines, chemical plants, and electrical components [3–6], as well as rechargeable batteries [7] and as a catalyst for specific chemical reactions [8, 9]. Nickel is also a crucial element in developing innovative alloys, including high- and medium-entropy alloys [10, 11].

Nickel’s abundant availability has prompted extensive research through both experimental and computational approaches. Commonly utilized density-functional theory (DFT) is a highly accurate, quantum mechanics-based atomistic simulation method. However, DFT’s efficiency is limited, making it computationally unaffordable to simulate complex defect properties, such as grain boundary migration, which demands simulations of over a thousand atoms and time scale exceeding 1 nanosecond. In nickel, the mechanical properties are considerably influenced by spin polarization, even weak itinerant ferromagnetism plays a role in affecting the antiphase boundaries [12]. Accounting for spin polarization further increases computational costs by a factor of ~ 3 .

Empirical or semi-empirical interatomic potentials are typically developed by fitting them to experimental and DFT data to accurately describe atomic environments for specific applications [13–16]. These potentials are computationally efficient and the computational speed usually scales linearly with the number of atoms. Over the past fifty years, dozens of Ni potentials have been developed (see in [17, 18]) and achieved many successes in explaining experimental observations and predicting material behaviors. However, the transferability

and accuracy of these potentials are limited by their fixed functional form and this concern becomes particularly acute regarding the properties of hexagonal close-packed (HCP) Ni. We benchmark the basic properties of face-centered cubic (FCC) and HCP Ni using various interatomic potentials, including 8 embedded-atom method (EAM) and 10 modified embedded-atom method (MEAM) potentials (see Supplementary Table S1). All potentials display significant discrepancies in the elastic constants (C_{ij}) of HCP Ni, possibly due to the limited fitting data. Specifically, these deviations can be as high as 54%, particularly in values C_{13} , C_{33} , and C_{44} . This indicates the challenge in accurately describing the plastic deformation behaviors of HCP Ni using these potentials, as well as related behaviors such as dislocation gliding and phase transformation. Indeed, allotropy phases significantly impact the strength/toughness of materials [19–22]. In polycrystalline nickel with a reduced grain size of ~ 17 nm through extensive plastic deformation [21, 23], 5–10% of grains exhibit an entire HCP structure, showing higher hardness and yield strength than perfect FCC grains [21]. Additionally, HCP Ni has been widely observed in extremely thin heteroepitaxial Ni films [24, 25]. The formation of HCP nickel remain insufficiently elucidated, and investigations into the FCC to HCP phase transformation in nickel are also limited [19, 21, 23, 24].

DFT calculations offer a comprehensive database of total energies, forces, and virial stresses for different crystal structures, enabling the development of potentials combined with machine learning (ML) methods for accurate description of individual allotropy phases [26]. One challenge in developing ML potential for Ni is addressing spin polarization. An ML spectral neighbor analysis potential (SNAP) was developed for Ni [27, 28], with training datasets derived from non-spin-polarized AIMD trajectories. This may be one reason why SNAP is unreliable for certain properties (as discussed in Section II). Fundamentally, ML potentials cannot capture the influence of magnetization on the free energy surface if there is no specific, well-defined descriptor for magnetic mo-

^{*} tongqwen@hku.hk

[†] srol@hku.hk

ments in the ML training. Efforts have been made to develop ML potentials that accurately assess magnetism, specifically for Fe and Mn-related systems [29–36]. Implementing these strategies can indeed result in a substantial improvement in the accuracy of potentials for quantifying magnetic moments and evaluating related properties. However, this implementation necessitates larger training datasets and increases training complexity. In many fields, the focus is on accurately predicting mechanical behavior while considering spin polarization, rather than the magnitude of intrinsic magnetism. Therefore, it is necessary to find a simple and effective training scheme to handle spin polarization to develop potentials with high accuracy and predictability.

In this study, we adopt a straightforward strategy to develop an ML deep potential (DP) [37] for Ni without using any descriptor for the magnetic moment, while considering the influence of spin polarization in the training datasets. The key lies in performing the spin-polarized calculations for all structures in the training dataset, including initial structures (static and AIMD simulations) and those explored during the DP-GEN loop [38] (see in Section IV C). Magnetic information serves as an implicit parameter in the neural network training. The resulting potential accurately reproduces basic properties of both FCC and HCP structures, which are explicitly included in the training dataset. Furthermore, this potential yields excellent flexibility and high accuracy in prediction, demonstrated by accurately predicting various defect properties and mechanical response behaviors that are outside the fitting dataset, such as point defects, stacking faults, dislocation cores, grain boundaries and ideal strength. We also employed this potential to investigate the allotropic phase transformation under mechanical loading. Consequently, the new potential enables predictive modeling of extensive mechanical behaviors of Ni and, in particular, serves as a tool to study more complex plastic transformation.

II. RESULTS AND DISCUSSION

Upon developing a DP model for Ni (DP-Ni), we systematically benchmark an extensive array of physical properties, including equation of states, elastic constants, finite temperature properties, phonon spectra, point defect energies, surface properties, plastic deformation, dislocation dissociation, and grain boundary energies. We compare the performance of DP-Ni model with widely-used and best-performed empirical/semi-empirical interatomic potentials, such as EAM by Y. Mishin *et al.* [39], MEAM.2021 by J.A.Vita *et al.* [40] and MEAM.2015 by W.-S. Ko *et al.* [41], and ML qSNAP potential by Y. Zuo *et al.* [27]. These benchmarks and comparisons serve to provide a comprehensive assessment of the performance and reliability of different interatomic potentials for both FCC and HCP Ni.

A. Basic Crystal Properties

Table I compares various properties among DFT, experiments, DP-Ni, and other interatomic potentials. In terms of lattice parameters and bulk energies, DP-Ni shows excellent agreement with both DFT and experimental values for stable FCC and metastable HCP structures. The energy difference between DP-Ni and DFT is within 3 meV/atom for both FCC and HCP Ni, while the lattice parameter difference between DP and DFT/experiment is within 0.004 Å. EAM and MEAM potentials also exhibit accurate lattice parameters for both phases, with discrepancies less than 2% when compared to DFT and experimental results. Regarding cohesive energy, DP-Ni slightly deviates from experimental value but accurately reproduces the DFT value for FCC Ni. EAM and MEAM.2015 potentials perfectly match the experimental cohesive energy of 4.450 eV/atom due to their exact fitting to the experimental value, while MEAM.2021 underestimates it by ~11%. In contrast, qSNAP potential exhibits a larger deviation of ~30% compared to experimental data. DP-Ni yields cohesive energy values almost identical to DFT calculations for the HCP phase. EAM and MEAM.2015 are close to experimental values, while other interatomic potentials significantly deviate from DFT or experimental results.

Elastic constants are fundamental material properties reflecting mechanical stability and strength. For accurate representation of mechanical behavior in large-scale atomistic simulations, it is essential for an interatomic potential to accurately reproduce the elastic constants of a material. In the case of FCC Ni, the largest discrepancy between DP and DFT/experiment is observed in C_{44} (2.3%)/ C_{11} (6.8%). All other interatomic potentials also accurately reproduce the elastic constants of FCC Ni, except for a slight underestimation of C_{44} for MEAM potentials. For HCP Ni, the predicted C_{ij} s of DFT and DP yield mechanical stability according to the criteria of $C_{11} - |C_{12}| > 0$, $(C_{11} + C_{12})C_{33} - 2C_{13}^2 > 0$ and $C_{44} > 0$ [47]. DP-Ni accurately reproduces the elastic constants of HCP Ni from DFT, with the maximum deviation at C_{12} (9.6%). However, all other potentials show large deviations in the elastic constants of HCP Ni compared to DFT results, particularly for EAM at C_{13} (37.4%), C_{33} (35.5%), and C_{44} (15.9%), and other three potentials at C_{44} (31.6%, 39.2%, 39.2% for MEAM.2021, MEAM.2015, and qSNAP, respectively). Elastic constants measure stress response to small applied strains, indicating sensitivity to locally distorted configurations. The training data for the DP-Ni includes many such distorted structures, obtained by slightly disturbing the equilibrium FCC and HCP configurations (see Section IV C). Consequently, DP-Ni accurately reproduces the elastic constants for both FCC and HCP phases. However, HCP phase information was not included in the fitting data of both classical potentials and ML qSNAP potential.

B. Phonon Spectra

In addition to mechanical stability criteria and cohesive energy, phonon spectra [49] serve as another method to predict

TABLE I. Comparison of different properties between DFT, experiment (Expt.), and various interatomic potentials. Lattice parameters (a), bulk energies (E), cohesive energies (E^{coh}), elastic constants (C_{ij}) of FCC and HCP Ni, and melting point of FCC Ni are from DFT, Expt., DP, EAM [39], MEAM_2021 [40], MEAM_2015 [41], and qSNAP [27]. Bold numbers indicate deviations of more than 15% compared to DFT and experiment.

Structure	Property	DFT	Expt.	DP	EAM	MEAM_2021	MEAM_2015	qSNAP
FCC	a (Å)	3.517	3.520 ^a	3.518	3.520	3.519	3.521	3.521
	E (eV/atom)	-5.467	-	-5.466	-4.450	-3.952	-4.450	-5.780
	E^{coh} (eV/atom)	4.875	4.450 ^b	4.862	4.450	3.952	4.450	5.780
	C_{11} (GPa)	275.7	261.2 ^c	278.9	247.9	278.3	260.4	267.5
	C_{12} (GPa)	156.0	150.8 ^c	158.1	147.8	169.8	148.6	155.3
	C_{44} (GPa)	130.7	131.7 ^c	127.7	124.8	112.5	111.1	125.7
	T_m (K)	-	1728 ^d	1635	-	-	1892	-
HCP	a (Å)	2.484	2.487 ^e	2.485	2.483	2.490	2.487	2.491
	c/a	1.643	1.645 ^e	1.641	1.619	1.630	1.642	1.643
	E (eV/atom)	-5.443	-	-5.446	-4.430	-3.956	-4.440	-5.772
	E^{coh} (eV/atom)	4.851	4.426 ^f	4.842	4.430	3.956	4.440	5.772
	C_{11} (GPa)	312.0	-	311.4	302.2	327.6	314.7	334.0
	C_{12} (GPa)	142.3	-	156.0	147.6	159.5	133.8	144.0
	C_{13} (GPa)	122.8	-	114.6	76.9	131.9	108.3	109.1
	C_{33} (GPa)	330.7	-	344.7	213.3	355.6	336.0	369.2
	C_{44} (GPa)	55.5	-	54.6	64.3	73.0	77.2	77.2

^a Lattice constants at 6 K from [42].

^b [43].

^c Experimental elastic constants at 0 K are extrapolated from low temperatures [44].

^d [45].

^e Lattice constants a and c/a ratio from room temperature [46].

^f This is calculated from the E^{coh} of FCC structure and the DFT energy difference between FCC and HCP.

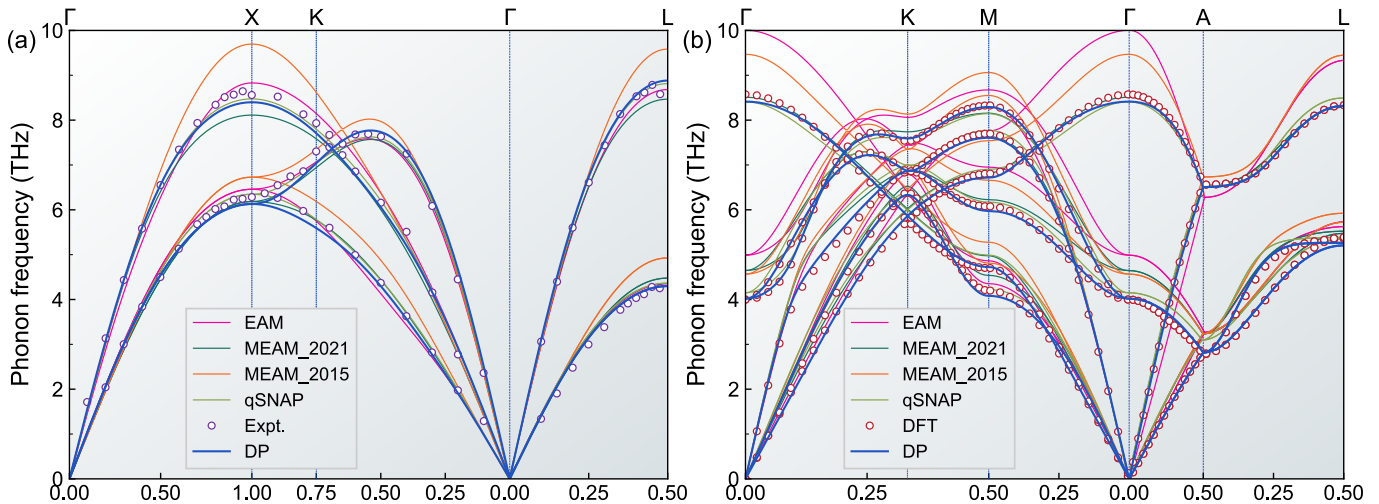


FIG. 1. Comparison of predicted and measured phonon spectra for (a) FCC and (b) HCP. The experimental values are from neutron diffraction at 298 K for FCC Ni [48], and the DFT data for HCP Ni is from this work.

and analyze crystal stability. Fig. 1 shows the phonon spectra of both FCC and HCP Ni obtained from experiment [48], DFT, DP-Ni, and other interatomic potentials. Both FCC and HCP Ni exhibit inherent stability as no imaginary frequencies are observed and all potentials qualitatively reproduce the profiles. However, notable variations in accuracy are observed among different potentials. DP-Ni demonstrates outstanding performance in both FCC and HCP crystal structures, reproducing all frequencies across the phonon spectra with high

accuracy. Minor deviations are observed in the qSNAP potential, particularly in the HCP structure. Other classical potentials exhibit evident deviations at frequency values at different symmetry points.

TABLE II. The calculated surface energies (E_s), interstitial formation energies (E_i^f), vacancy formation energies (E_v^f), and unstable (γ_{usf}) and stable stacking fault energies (γ_{sf}), as well as grain boundary energies of low Miller index tilt boundaries for FCC Ni using DP-Ni, in comparison with DFT results, available experimental data, and selected interatomic potentials. \otimes , \odot , \ddagger , \oplus represent that the initial interstitial structures are not stable and will transform to $\langle 110 \rangle$ dumbbell, tetrahedral, $\langle 100 \rangle$ dumbbell, and $\langle 111 \rangle$ dumbbell after full relaxation, respectively. Bold numbers indicate over 15% biases compared to DFT/Expt.

Property	DFT	Expt.	DP	EAM	MEAM_2021	MEAM_2015	qSNAP
$E_s\{111\}$ (J/m ²)	1.919		1.958	1.636	1.815	1.630	1.938
$E_s\{221\}$ (J/m ²)	2.210		2.259	1.924	2.164	1.965	2.230
$E_s\{110\}$ (J/m ²)	2.343	2.240 ^a	2.357	2.056	2.367	2.172	2.356
$E_s\{211\}$ (J/m ²)	2.279		2.323	1.970	2.222	2.021	2.280
$E_s\{210\}$ (J/m ²)	2.463		2.488	2.181	2.526	2.321	2.472
$E_s\{100\}$ (J/m ²)	2.239		2.223	1.884	2.220	2.088	2.254
E_v^f (eV)	1.365	1.400–1.800 ^b	1.242	1.600	1.545	1.510	1.470
E_i^f $\langle 100 \rangle$ dumbbell (eV)	4.047	-	4.184	4.911	4.329	4.611	4.195
E_i^f $\langle 111 \rangle$ dumbbell (eV)	4.664	-	4.920	5.800	4.824	5.194	\ddagger
E_i^f $\langle 110 \rangle$ dumbbell (eV)	4.828	-	4.633	\ddagger	\odot	\oplus	\ddagger
E_i^f Crowdion (eV)	\otimes	-	\otimes	5.120	4.329	\oplus	\ddagger
E_i^f Octahedral (eV)	4.229	-	4.529	5.397	4.571	4.611	\ddagger
E_i^f Tetrahedral (eV)	4.670	-	5.001	6.915	4.725	5.558	\ddagger
γ_{usf} $\langle 110 \rangle$ (mJ/m ²)	766.6	-	801.6	924.3	746.9	898.2	789.9
γ_{usf} $\langle 112 \rangle$ (mJ/m ²)	280.4	-	301.9	365.6	285.4	423.6	275.5
γ_{sf} $\langle 112 \rangle$ (mJ/m ²)	135.9	125 ^c	126.8	125.2	-26.9	60.0	52.2
$\Sigma 3$ $[1\bar{1}0]$ (111) (mJ/m ²)	68.03	-	63.50	63.46	-13.45	30.09	26.53
$\Sigma 3$ $[1\bar{1}0]$ (112) (mJ/m ²)	896.02	-	893.67	1064.03	782.53	960.66	908.44
$\Sigma 5$ $[100]$ (021) (mJ/m ²)	1288.75	-	1310.72	1564.08	1372.11	1421.66	1339.00
$\Sigma 7$ $[111]$ (321) (mJ/m ²)	1234.31	-	1212.57	1471.91	1210.14	1395.51	1286.36
$\Sigma 9$ $[1\bar{1}0]$ (221) (mJ/m ²)	1120.58	-	1103.69	1368.13	1148.89	1258.83	1157.30
$\Sigma 11$ $[1\bar{1}0]$ (113) (mJ/m ²)	454.23	-	440.81	531.15	420.36	518.89	464.21

^a Average orientation [50]

^b [51]

^c [52, 53]

C. FCC Surface Energies and Point Defects

In Table II, the surface formation energies of low Miller index surfaces calculated by DP-Ni are compared to values obtained from DFT, available experiments, and four other potentials. Our DFT results are consistent with both the values and ordering of the previous DFT calculations [54]. DFT predicts that the $\{111\}$ close-packed plane has the lowest surface energy, while $\{210\}$ plane yields the highest. All interatomic potentials successfully reproduce the lowest and highest energy planes. DP-Ni results show excellent agreement with DFT, exhibiting a maximum error of 2.2% for the $\{221\}$ plane. MEAM_2021 and qSNAP potentials also provide accurate predictions (errors within 6%). However, EAM and MEAM_2015 potentials slightly overestimate the surface energy by 11.4%-15.9% and 5.8%-15.1%, respectively. The given experimental value 2.240 J/m² is derived from the average orientation [50]. The vacancy formation energy (E_v^f) of DP-Ni is ~ 0.124 eV (-9.0%) lower than the DFT value. All other potentials yield higher values than the DFT E_v^f results, but they remain within the range of experimental values.

The FCC structure displays six types of self-interstitial configurations based on geometry, namely the $\langle 100 \rangle$ dumbbell, $\langle 111 \rangle$ dumbbell, $\langle 110 \rangle$ dumbbell, crowdion, octahedral, and

tetrahedral, as seen in Supplementary Fig. S1. According to our DFT calculations, $\langle 100 \rangle$ dumbbell has the lowest formation energy in FCC Ni, followed by octahedral, $\langle 111 \rangle$ dumbbell, tetrahedral, and $\langle 110 \rangle$ dumbbell. The crowdion configuration relaxes to the $\langle 110 \rangle$ dumbbell. This energy ordering is consistent with results in Refs. [55–57]. Due to the high efficiency of interatomic potentials, here we utilize $10 \times 10 \times 10$ supercell to calculate the self-interstitial formation energies. DP-Ni can capture all the metastable configurations, and the maximum difference is less than 7.1% (octahedral) compared to DFT results. However, a small inconsistency with DFT is the altered energy ordering sequence for DP, which is (from low to high): $\langle 100 \rangle$ dumbbell, octahedral, $\langle 110 \rangle$ dumbbell, $\langle 111 \rangle$ dumbbell and tetrahedral. Other potentials can accurately capture the lowest energy structure of $\langle 100 \rangle$ dumbbell but yield diverse results for other metastable configurations. Notably, all interstitial structures relax to the $\langle 100 \rangle$ dumbbell using the qSNAP potentials.

It is worth mentioning that the training datasets for the DP-Ni potential do not explicitly encompass vacancy and self-interstitial configurations. Nonetheless, DP-Ni demonstrates exceptional transferability and representability in basic material properties. This implies that DP-Ni is capable of accurately capturing and reproducing essential characteristics of Ni, even for situations not explicitly included in the training

data. This underscores the versatility and reliability of the DP-Ni model in predicting and modeling various material properties.

D. Cohesive and Decohesive Energy

The relationship between cohesive energy and atomic spacing is crucial for determining various mechanical properties, such as tensile and compressive behaviors. DFT often generates a smooth cohesive energy curve, suggesting gradual and continuous energy variation with atomic positions. Fig. 2 displays the cohesive curves for FCC Ni at 0 K, calculated by DFT and various interatomic potentials. The curves generated by DFT, DP-Ni, MEAM_2021, and MEAM_2015 exhibit smoothness across the entire range. Notably, the DP-Ni and DFT curves overlap, while MEAM_2015 deviates from the DFT value around the equilibrium lattice parameter. In contrast, MEAM_2021 shows large deviations from the DFT curve within the $0.5a_0$ to $2a_0$ range. The EAM curve remains continuous at large atom separations but exhibits discontinuities under large compression, with deviations from the DFT curve within the $1.25a_0$ to $2a_0$ range. The qSNAP potential yields a discontinuous and inaccurate cohesive energy line and its cohesive energy for equilibrium FCC Ni substantially deviates from the DFT results (also seen in Table I). This indicates that the qSNAP potential may introduce unexpected and significant errors in properties related to mechanical response.

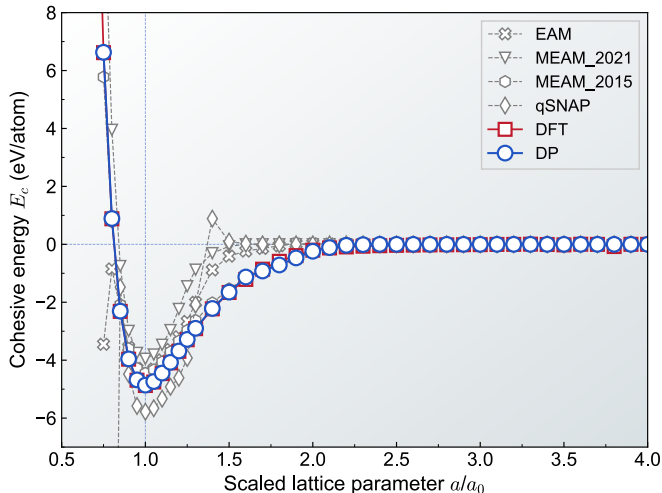


FIG. 2. The cohesive energy of FCC Ni as a function of lattice parameter calculated by DFT and various interatomic potentials.

Examining the surface decohesion energy and its gradient (stress) provides a deeper understanding of the energy landscape and cohesive forces involved in atomic plane separation. This is crucial for predicting and simulating fracture processes, such as crack propagation and material failure. Fig. 3 displays the surface decohesion energy and its gradient for four crystallographic planes using DFT and different interatomic potentials. It should be emphasized that no plane separation configuration is explicitly included in the DFT train-

ing datasets of DP-Ni. The DP-Ni model demonstrates desirable predictability, with smooth decohesion energy and stress contours closely aligned with DFT values for all planes. The MEAM_2021 and qSNAP potentials also show relatively good agreement with DFT data. However, significant deviations in energy and stress are observed for separation distance (d) ranging from 0.5 \AA to 3 \AA for $\{100\}$, $\{110\}$, $\{112\}$ planes and 0.5 \AA to 2.5 \AA for $\{111\}$ plane. Additionally, the peak stress position for qSNAP shifts to the right at around $d = 1 \text{ \AA}$. The EAM potential exhibits discontinuities for $\{100\}$, $\{110\}$, $\{111\}$ planes within the range of $d = 1.5 \text{ \AA}$ to $d = 3.5 \text{ \AA}$, leading to fluctuating decohesion stresses. For all planes, the EAM decohesion energies are much smaller than DFT when $d > 1.5 \text{ \AA}$. All peak stress positions for the EAM potential shift to the left at around $d = 0.4 \text{ \AA}$. As for MEAM_2015 potential, it closely aligns with DFT results for all cases, except for abrupt jumps observed at $d = 2.5 \text{ \AA}$.

E. Ideal Strength

Smooth cohesive and decohesive energies are crucial for the accurate description of mechanical behavior, especially concerning the ideal strength. Ideal strength refers to the maximum stress that a perfect material can withstand before undergoing plastic deformation or failure [58]. This property can be identified through the stress-strain curve, which serves as a valuable tool for material application and design. Here, we initially assess the ideal strength of FCC Ni under tensile and shear loading using DFT calculations. Fig. 4 shows the computed stress as a function of applied strain in various directions, revealing two distinct elastic and plastic regions. In the elastic strain region, stress increases linearly with low strain. In contrast, at higher strains, the material demonstrates clear plastic characteristics, with the maximum ideal strength (σ_{ideal}) attained at a specific strain value (ϵ_{ideal}). It is worth noting that the stress-strain curves exhibit significant anisotropy. For example, the σ_{ideal} and ϵ_{ideal} differ considerably between the $[001]$ and $[011]$ directions under the uniaxial tension. Additionally, the $(111)\langle 112 \rangle$ directions under shear stress show obvious “hard” and “easy” characteristics, the σ_{ideal} and ϵ_{ideal} values can vary due to the asymmetric geometries. Overall, Ni exhibits 29.0 GPa of σ_{ideal} and 0.52 of ϵ_{ideal} under the hydrostatic condition. The maximum σ_{ideal} and ϵ_{ideal} for uniaxial tension are 35.3 GPa and 0.41 along the $[001]$ direction, while for shear, they are 15.9 GPa and 0.28 along the $(111)[\bar{1}\bar{1}2]$ direction.

Unlike the calculation of elastic constants, calculating ideal strength involves significant deformation, posing considerable demands on the potential function’s ability to accurately describe plastic deformation across a wide range of strains. We conducted a comparative analysis of stress-strain relationships among various interatomic potentials using single-point calculations with DFT relaxed configurations. DP-Ni demonstrates high accuracy compared to DFT results, especially for hydrostatic and $[111]$ uniaxial tension, as well as shear of $(111)[1\bar{1}0]$, $(111)[\bar{1}10]$ and $(111)[11\bar{2}]$. The largest deviations observed are 10.4% and 9.3% in the plastic deformation

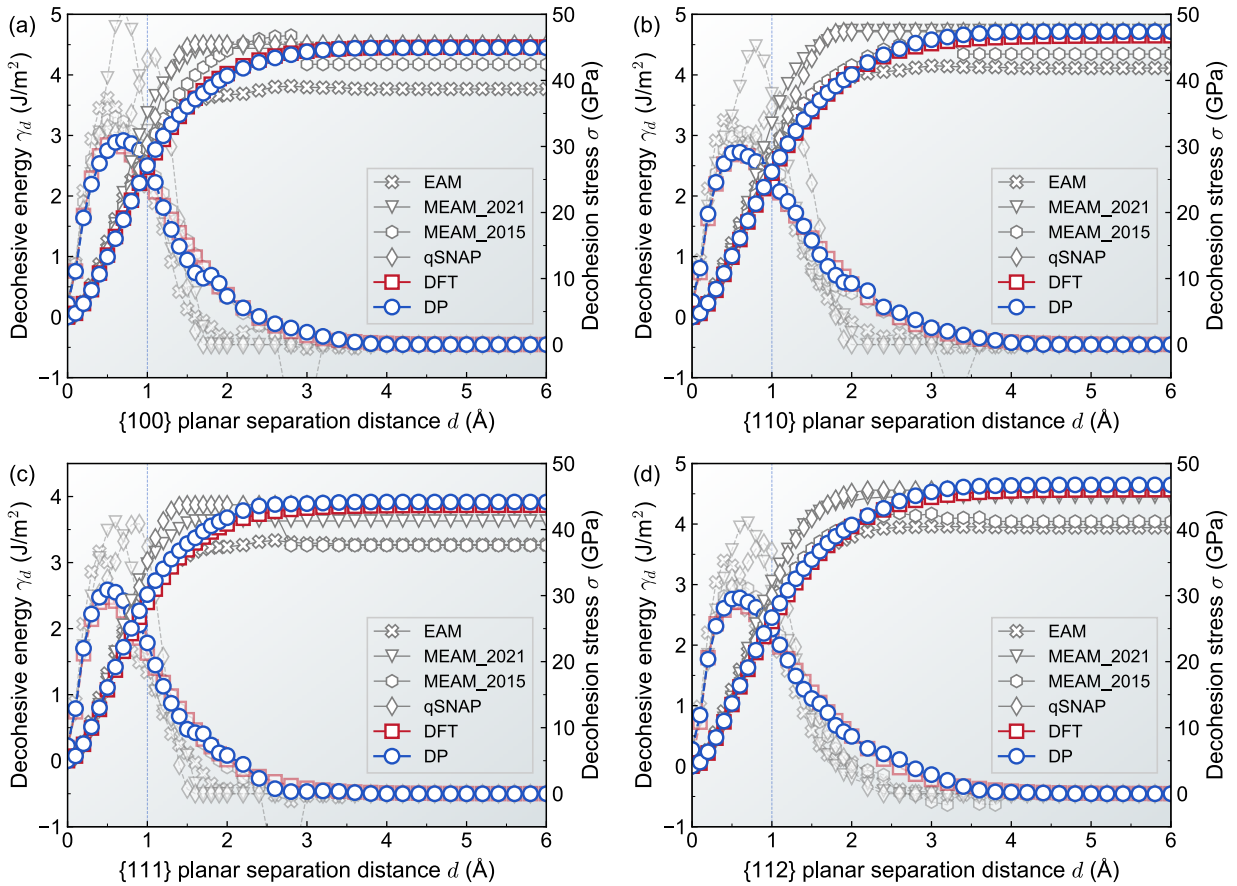


FIG. 3. The plane decohesion energy (γ_d) and stress (σ) as a function of plane separation distance (d) for (a) $\{100\}$, (b) $\{110\}$, (c) $\{111\}$ and (d) $\{112\}$ planes.

region for $[011]$ tension and $(111)[\bar{1}\bar{1}2]$ shear, respectively. DP-Ni also reproduces the ϵ_{ideal} in all cases. MEAM_2021 performs well in shear cases but overestimates ideal strength and strain in hydrostatic and uniaxial tension cases. Similarly, qSNAP shows good performance in shear cases but overestimates σ_{ideal} and underestimates ϵ_{ideal} under hydrostatic and most uniaxial tensions. The EAM model shows large deviations in stress and strain compared to DFT results, with the most prominent discrepancy being a 58.7% deviation under tension loading along the $[011]$ direction. The secondary reinforcement is particularly noticeable under hydrostatic tension. In comparison to DFT results, the MEAM_2015 potential displays minor discrepancies in hydrostatic and most uniaxial tensions but overestimates the ideal strength in all shear cases.

F. Finite Temperature Properties

Nickel, a component in widely-used superalloys, is often exposed to high-temperature environments. Large-scale MD simulations can accurately describe finite-temperature properties, offering valuable physical insights and enhancing our understanding of relevant behavior. Fig. 5 shows the lattice parameters and elastic constants of FCC Ni at different tem-

peratures, as calculated by DFT and different interatomic potentials. For lattice parameter a , DP-Ni and other potentials demonstrate a linear increase from 0 to 1700 K. Notably, the lattice parameter from DP-Ni closely aligns with experimental results at high temperatures (above 600 K) [59]. Furthermore, the thermal expansion coefficients (slope) of DP-Ni are similar to experimental values. The melting point of Ni, calculated to be 1635 K (± 5 K) by DP (Table I) using two-phase method, is $\sim 5.3\%$ lower than the experimental value (1728 K). Figs. 5(b)-(d) display the elastic constants C_{ij} as a function of temperature from DFT and various potentials. DP-Ni results exhibit a continuous decrease with increasing temperature and good agreement with DFT/experiment [60, 61], particularly for C_{11} and C_{44} . Other potentials reveal different trends or profiles compared to DFT/experiment. EAM shows an increase of C_{ij} with temperature below 400 K, followed by a continuous decrease with increasing temperature. This abnormal behavior of elastic constants is also observed for MEAM_2021 and qSNAP for C_{12} . MEAM_2015 displays a reasonable trend compared to DFT/experiment across the entire temperature range, but the discrepancy between MEAM_2015 and experiment is significant (over 15%) for C_{12} when the temperature exceeds 600 K. The unreliability of empirical potentials and ML qSNAP potential at finite temperatures is unexpected, indicating that these potentials are

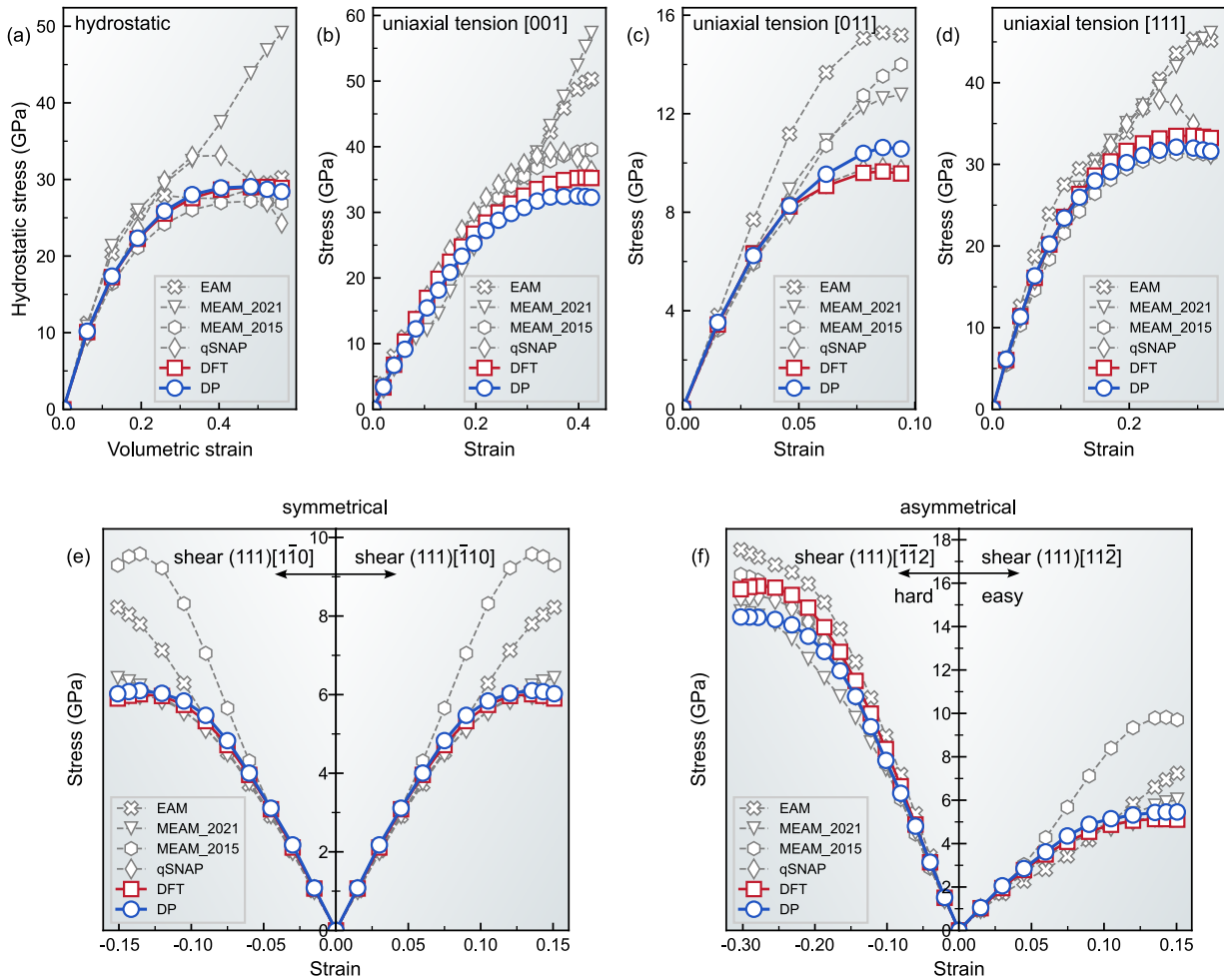


FIG. 4. Stress-strain curves for (a) hydrostatic, (b) [001], (c) [011], (d) [111] uniaxial tensions as well as (e) (111)[$\bar{1}\bar{1}0$], (111)[$\bar{1}\bar{1}0$], (f) (111)[$\bar{1}\bar{1}2$], (111)[$11\bar{2}$] shear deformations.

insufficient for modeling various material behavior at finite temperatures.

G. Stacking Fault and Dislocation Core

The generalized stacking fault energy (GSFE) is a critical surrogate property for predicting the mechanical behavior of materials, including dislocation and twinning properties [62]. GSFE represents the energy required for crystal lattice planes to undergo relative slip under shear stress, leading to the formation of stacking faults. This energy is determined by initiating a displacement from a reference point and sliding it along a specific direction, resulting in a displacement fault energy curve called the γ -line [63]. The maximum energy value along the γ -line corresponds to the unstable stacking fault energy (γ_{usf}), which dictates the barrier for dislocation nucleation at stress concentrations like crack tips. The metastable point on the γ -line, referred to as γ_{sf} , determines the dissociation of dislocations. When considering a complete two-dimensional plane for slip, all the γ -lines collec-

tively create a two-dimensional profile known as the γ -plane or γ -surface [63].

Figs. 6(a)-(b) show the γ -lines along the $\langle 110 \rangle/2$ and $\langle 112 \rangle/2$ directions on the $\{111\}$ plane with the loosest packing, calculated by DFT and different interatomic potentials. In DFT calculations, only an unstable stacking fault is observed along the $\langle 110 \rangle/2$ direction with a γ_{usf} of 766.6 mJ/m² at half of the Burger vector $\mathbf{b}-\langle 110 \rangle/2$, consistent with previous DFT calculations [64]. For the $\langle 112 \rangle/2$ slip direction, a stable stacking fault occurs at $\mathbf{b}/3$ ($\mathbf{b}=\langle 112 \rangle/2$) while an unstable stacking fault is present at $\mathbf{b}/6$. Although a peak appears at $2\mathbf{b}/3$ in the γ -line, it is irrelevant due to the high barrier of 1168.4 mJ/m², which prevents atom slip. The DFT calculations yield γ_{usf} and γ_{sf} values of 280.4 mJ/m² and 135.9 mJ/m², respectively. The γ_{sf} is in good agreement with experimental results (125 mJ/m² [52, 53]) and previous DFT values ranging from 110 to 145 mJ/m² [64, 65]. Figs. 6 (a) and (b) also display γ -line results from DP-Ni and other interatomic potentials. All potentials reproduce the general shape of the γ -lines from DFT except for MEAM_2015, which shows a minimum value at $\mathbf{b}/2$ along $\langle 110 \rangle/2$ direction. Table II lists the calculated γ_{usf} and γ_{sf} values. DP-Ni reproduces differ-

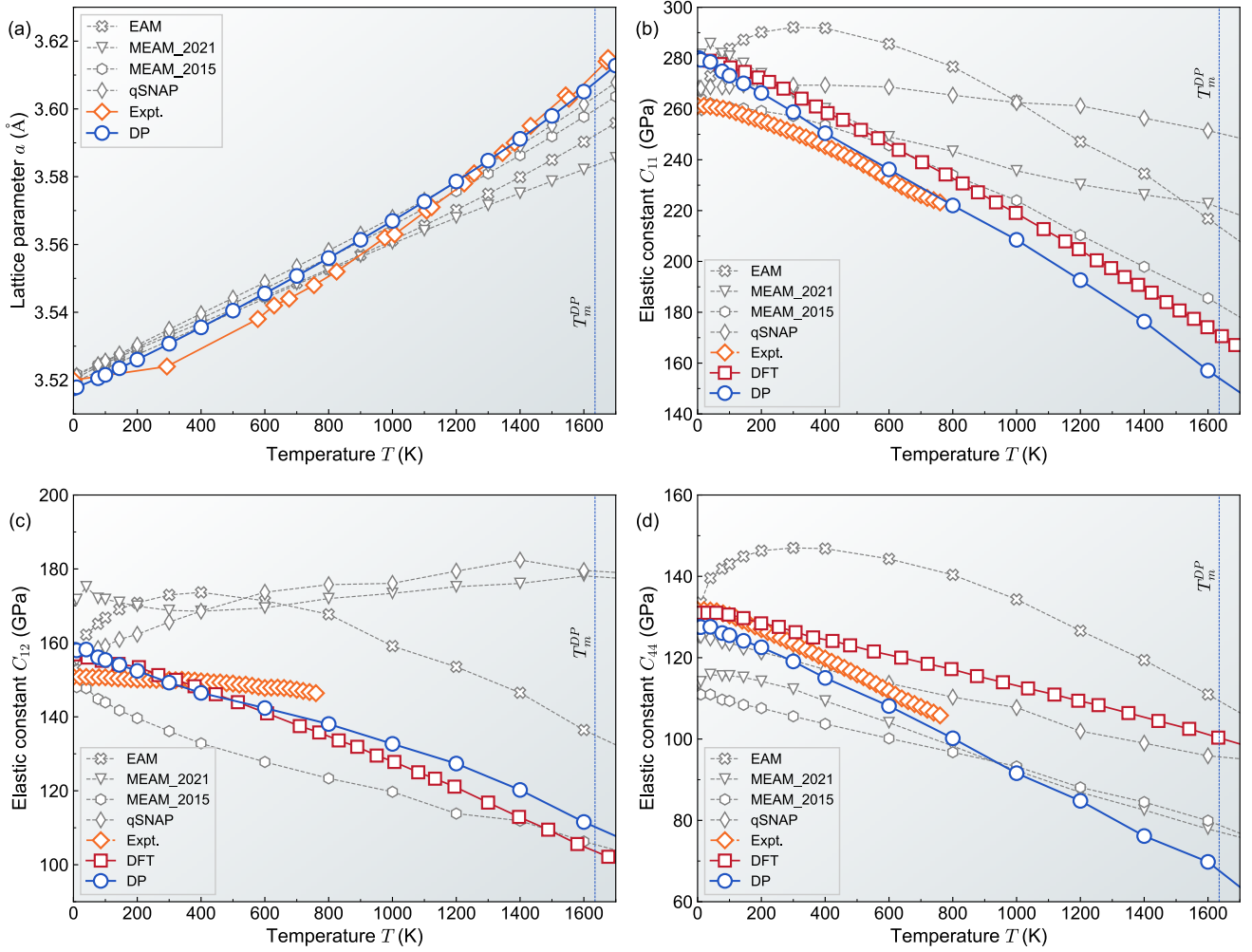


FIG. 5. Finite-temperature properties of FCC Ni calculated from DFT, DP-Ni and other potentials. (a) lattice parameters and elastic constants (b) C_{11} , (c) C_{12} and (d) C_{44} . The experimental values of lattice parameters are from Ref. [59], while the DFT and experimental data of elastic constants are from Refs. [60] and [61], respectively.

ent stacking fault energies well compared to DFT results, with deviations of only 4.6% for γ_{usf} in the $\langle 110 \rangle/2$ slip, 7.6% for γ_{usf} and 6.7% for γ_{sf} along the $\langle 112 \rangle/2$ slip. Notably, there are no special configurations regarding stacking faults in the training datasets, indicating excellent transferability and representability of DP-Ni. In contrast, MEAM_2021 and qSNAP potentials capture the γ_{usf} well in both $\langle 110 \rangle/2$ and $\langle 112 \rangle/2$ directions, but significantly underestimate the γ_{sf} , particularly for MEAM_2021 which yields a negative γ_{sf} . While the EAM potential accurately describes the γ_{sf} , it overestimates both γ_{usf} in $\langle 110 \rangle/2$ and $\langle 112 \rangle/2$ directions. MEAM_2015 potential fails to accurately describe both γ_{usf} and γ_{sf} . Based on these unexpected results about GSFE from the empirical and ML qSNAP potentials, it is predicted that these potentials will struggle to accurately simulate dislocation nucleation and dislocation dissociation behavior. To display the minimum energy path on the $\{111\}$ plane, Fig. 6(c) plots the γ -surface of DP-Ni. The γ -surface on the $\{111\}$ plane exhibits the expected symmetry from geometry and no energy singularity. The minimum energy path should follow the green or red

dashed arrows (Fig. 6(c)), indicating that a full dislocation $\langle 110 \rangle/2$ or $\langle 112 \rangle/2$ will dissociate into partials in the $\{111\}$ plane.

In FCC metals, full dislocations dissociate into Shockley partial dislocations with a stable stacking fault in between to reduce elastic energy [69]. Accurate modeling of dislocation dissociation and separation distance is essential for precise modeling of plastic behavior. Initially, we insert a perfect $\langle 110 \rangle/2$ edge and screw dislocation at the center of $301 \times 17 \times 85 \text{ \AA}^3$ (dislocation line is along the y direction, namely the dimension of 17 \AA , while Burgers vector parallels the x direction, namely the dimension of 301 \AA) and $15 \times 302 \times 85 \text{ \AA}^3$ (dislocation line and Burgers vector parallel the x direction, namely the dimension of 15 \AA) supercells with periodic boundary conditions, respectively. Following this, we perform energy minimization using molecular statics simulation at 0 K with DP-Ni, and Fig. 7 shows the relaxed configurations. The edge and screw configurations have two Shockley partial dislocations with different separation distances. The differential displacement (DD) [70] plot reveals the strain fields

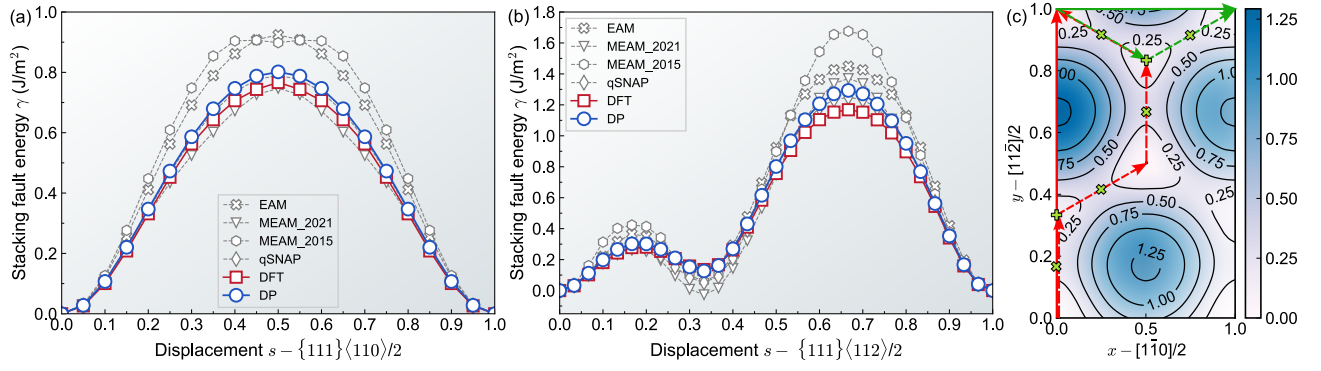


FIG. 6. Generalized stacking fault energy (GSFE) lines (γ -lines) along the (a) $\langle 110 \rangle / 2$ and (b) $\langle 112 \rangle / 2$ directions, as well as (c) GSFE surfaces (γ -surface) on the loosest packing $\{111\}$ planes predicted by DP-Ni. The solid red and green arrows represent the slip path along $\langle 112 \rangle / 2$ and $\langle 110 \rangle / 2$ directions respectively, and dashed arrows show the corresponding dissociated slip paths. The symbols of + and \times represent the positions of stable and unstable stacking faults.

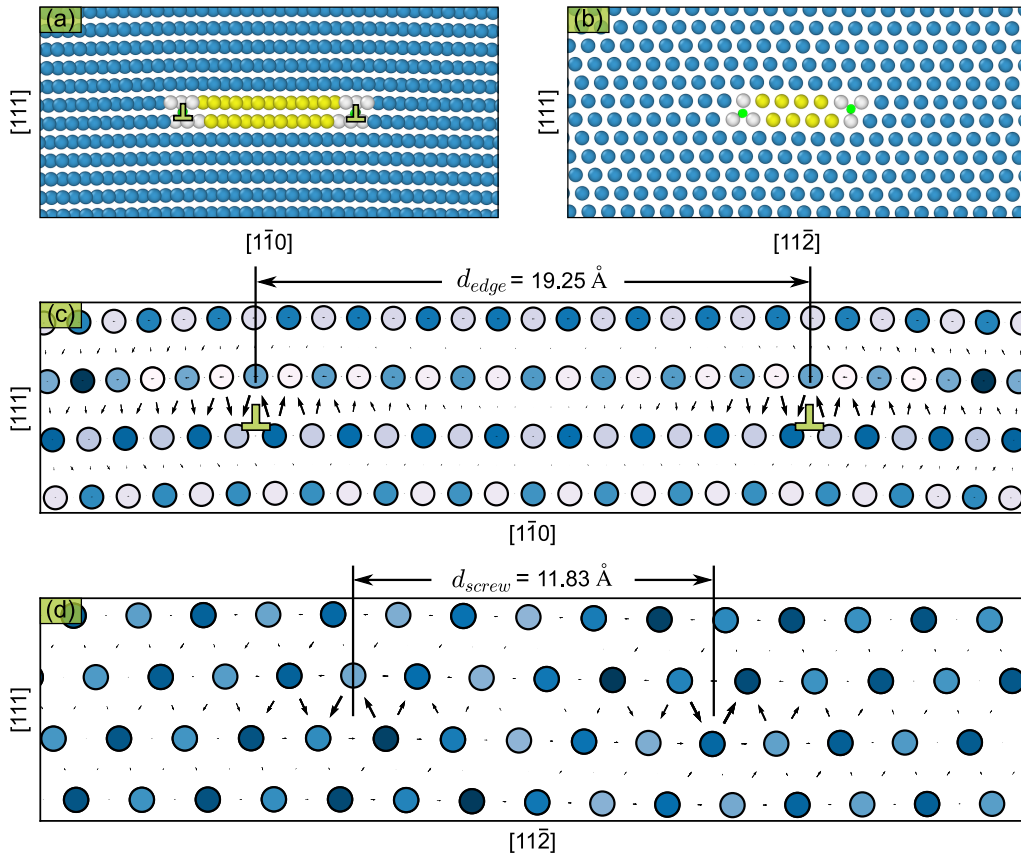


FIG. 7. Dislocation core structures of two Shockley partials of $\langle 110 \rangle / 2$ edge and screw dislocations in FCC Ni predicted by DP-Ni. (a) and (b) show the atomic configurations of edge and screw dislocations visualized by OVITO [66]. The common neighbor analysis (CNA) method [67] is utilized to distinguish the FCC (blue), HCP (yellow), and other (white) local atom stacking. The dislocation extraction algorithm (DXA) [68] is employed to identify dislocations precisely. (c) and (d) show the corresponding differential displacement plots for (a) and (b). The partial core separations are shown to be d_{edge} and d_{screw} of 19.25 \AA and 11.83 \AA .

around a dislocation by measuring the relative displacement of two nearest neighbor atoms. A partial dislocation consists of three atoms with clockwise or counterclockwise net chirality in their three vectors. In this case, the DD plots in Figs. 7(c) and (d) further identify the positions of partial dislocations.

The predicted partial dislocation separation distances d_{edge} and d_{screw} are 19.25 \AA and 11.83 \AA , respectively. Our result for the edge dislocation separation distance aligns with weak-beam transmission electron microscopy, which evaluated a range of $26 \pm 8 \text{ \AA}$ [52]. While d_{screw} is not easily ob-

served experimentally, our result of 11.83 Å is consistent with the 12.0 Å by DFT calculations [71].

H. Structures and Energies of Tilt Grain Boundaries

Grain boundary (GB) defects are ubiquitous in polycrystalline materials and play a crucial role in determining mechanical properties such as strength and ductility. In this study, we investigate several tilt GBs with coincident site lattice (CSL) structure under low Miller index. The initial GB structures are ideal configurations with two symmetric grains situated along the GBs. We identify the lowest energy structures by displacing one grain relative to another one during energy minimization. The lowest-energy GB configurations after relaxation by DP-Ni are plotted in Fig. S2. The relaxed $\Sigma 3$ $[1\bar{1}0]$ (111), $\Sigma 5$ $[100]$ (021) and $\Sigma 11$ $[1\bar{1}0]$ (113) maintain symmetric configurations, exhibiting twinning structures, while $\Sigma 3$ $[1\bar{1}0]$ (112), $\Sigma 7$ $[111]$ (321) and $\Sigma 9$ $[110]$ (221) relax to asymmetric boundary structures. Table II presents the GB energies calculated by DFT and different interatomic potentials. DP-Ni accurately reproduces all GB energies with minor discrepancies (less than 6.7%) compared to the respective DFT values. Both DP-Ni and DFT identify $\Sigma 3$ $[1\bar{1}0]$ (111) as the lowest GB energy, aligning with most experimental observations [72]. The energy ordering follows the pattern: $\Sigma 3$ (111) < $\Sigma 11$ < $\Sigma 3$ (112) < $\Sigma 9$ < $\Sigma 7$ < $\Sigma 5$. Other potentials capture the energy ordering of these GBs but are less reliable for GB energies. EAM accurately predicts the energy of $\Sigma 3$ $[1\bar{1}0]$ (111), but overestimates other GB energies in the range of 16.9%-22.1%. MEAM_2021, MEAM_2015 and qS-NAP roughly reproduce the energy of high Σ GBs but drastically underestimate the energy of $\Sigma 3$ $[1\bar{1}0]$ (111) (over 50%), particularly for the negative value by MEAM_2021. Overall, DP-Ni reproduces all GB structures and corresponding energies, demonstrating its potential for future studies of various GB motions, such as twin nucleation induced by deformation, GB migration, and interaction with disconnections [73–75].

I. Allotropic Transformation of Nickel under Uniaxial Tension

In this section, we analyzed the allotropic phase transformation of nickel during mechanical deformations using DP-Ni. Fig. 8 illustrates the stress-strain relationship under uniaxial tension along the $[001]$ crystallographic direction and calculations were conducted at 0 K using a single unit cell. To enhance visual clarity, atomic configurations in Fig. 8 have been replicated. The results show a monotonic increase in stress as a function of strain, followed by a sudden decrease at the strain of ~ 0.226 . The inset atomic configuration depicts the morphological evolution from FCC to HCP structures. A closer examination of the deformation mechanism reveals that the FCC phase remains stable until the strain reaches $\sim 22.6\%$. Beyond this critical strain threshold, the FCC nickel loses stability and undergoes a rapid transition to the HCP phase. Subsequently, the HCP phase maintains stability for an additional strain of roughly 15% (from point B).

We observe that the transformation strain exhibited is considerably larger than the typical values for common phase transformations, which generally fall below 15% [76–80]. However, such extensive transformation strains are not unusual for FCC metals, as they have been documented to undergo significant strain during phase transitions. This observation is supported by both experimental observations and theoretical calculations [81–87]. Specifically, in the case of nickel, it was highlighted by experiments that HCP nanograins form within the polycrystal as plastic strain accumulates [21, 23]. To confirm this transformation, the energy differences (ΔE) between structures at points A and B were quantified, as shown in Fig. 8. The positive values obtained from both the DP-Ni and DFT calculations suggest that the HCP structure at point B is more stable compared to the strained FCC structures at point A. We apply DFT to calculate the stress of the structures in the strain-stress curve from DP-Ni. As indicated by the red squares in Fig. 8, the results from DP-Ni are very close to those from DFT. At the moment of allotropic transformation, the energy discrepancies, ΔE_{DP} and ΔE_{DFT} , are as small as 0.012 eV/atom, corroborating the fidelity of the DP-Ni model. The observed crystallographic orientation relationship between FCC and HCP structures in our study presents an atypical case, namely, $\{100\}_{\text{FCC}} \parallel \{0001\}_{\text{HCP}}$ and $\langle 010 \rangle_{\text{FCC}} \parallel \langle 11\bar{2}0 \rangle_{\text{HCP}}$. This orientation deviates from the commonly documented strain-induced FCC-HCP transformation, which is typified by the orientation relation of $\{111\}_{\text{FCC}} \parallel \{0001\}_{\text{HCP}}$ and $\langle 1\bar{1}0 \rangle_{\text{FCC}} \parallel \langle 11\bar{2}0 \rangle_{\text{HCP}}$, as reported in previous studies [19, 22, 81, 88]. The rationale for this aberration is ascribed to the phase transformation occurring under conditions of high strain and stress, which facilitate a propensity for orientation modification during such pronounced deformation. Moreover, this orientation relationship is corroborated by other theoretical [82, 89] and experimental investigations [90] in other FCC metals. Additionally, another unconventional instance is manifested in nanograined nickel, where the orientation relationship $\langle 110 \rangle_{\text{FCC}} \parallel \langle 1\bar{2}1\bar{3} \rangle_{\text{HCP}}$ has been identified experimentally [21].

III. CONCLUSION

In summary, we developed a machine learning Deep Potential (DP) model for accurately representing mechanical properties in magnetic nickel allotropy, including both FCC and HCP phases. The nickel DP (DP-Ni) is directly fitted to spin-polarized DFT calculations using a small training datasets consisting of 2020 frames (see Supplementary Table S2). DP-Ni achieves DFT-level accuracy in predicting various properties for both FCC and HCP Ni, such as (finite-temperature) lattice parameters and elastic constants, phonon spectra, cohesive and decohesive energies, point defect formation energies, and dislocation and grain boundary properties. DP-Ni thus serves as a promising tool for large-scale atomistic simulations of the mechanical behavior of Ni. Our DP-Ni model facilitated the examination of the allotropic phase transition, wherein we identified a high critical strain and an atypical orientation relationship during the FCC-HCP transfor-

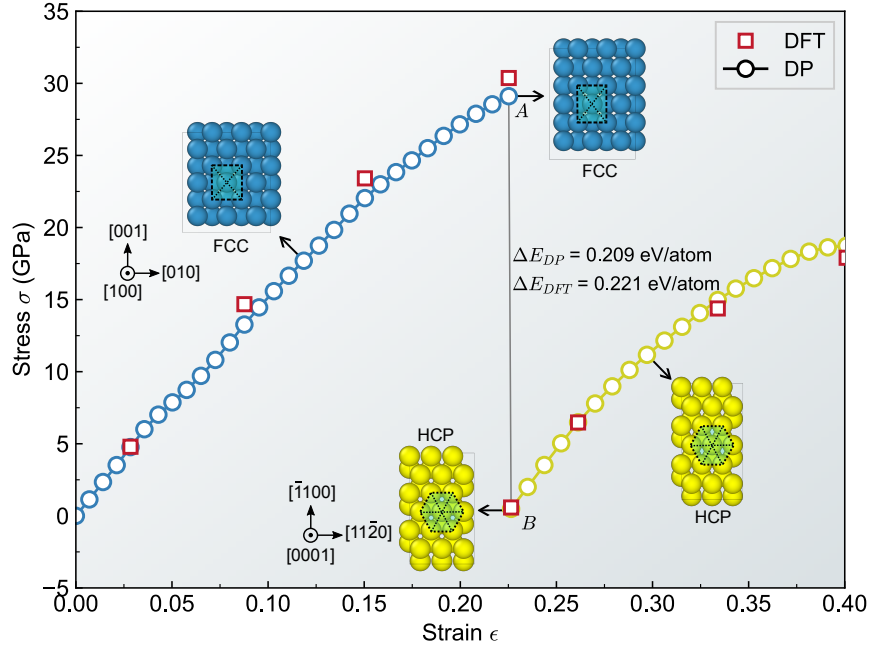


FIG. 8. The uniaxial stress vs. strain of Ni under uniaxial tension along [001] using DP-Ni at 0 K. The red square points are the stress calculated by DFT under the corresponding strain. Allotropic phase transformation is induced upon a precipitous decrease in stress. The energy difference values represent the cumulative energy discrepancy of structures at points A and B as computed by the DP-Ni and DFT, respectively. The insert atomic configurations are labeled using CNA [67] for FCC (blue) and HCP (yellow) local packing by OVITO [66]. The crystallographic orientation relationship for FCC-HCP is $\{100\}_{\text{FCC}}\|\{0001\}_{\text{HCP}}$ and $\langle 010\rangle_{\text{FCC}}\|\langle 11\bar{2}0\rangle_{\text{HCP}}$.

mation under uniaxial tensile loading. Future directions include investigating phase transformations in polycrystal, grain boundary mobility, and designing mechanical properties by tailoring grain boundary microstructures. Furthermore, DP-Ni and the training datasets can be utilized as a foundation for developing ML potential for Ni-based superalloys, medium-entropy alloys (FeCoNi), and high-entropy alloys (FeCoNi-based) through methods such as the DP attention pre-training model [91].

IV. METHODS

A. DFT Calculations

The Vienna Ab initio Simulation Package (VASP) [92, 93] is used to perform all the density functional theory (DFT) calculations by employing the projector augmented wave (PAW) method [94]. The exchange-correlation functional is treated within the generalized gradient approximation (GGA) formulated by Perdew-Burke-Ernzerhof (PBE) [95]. Valence electrons in the calculations consist of the outer 10 electrons ($3d^84s^2$) of Ni. A plane wave cutoff energy of 600 eV is chosen for the plane-wave expansion of the electronic wavefunctions. The Methfessel-Paxton method [96] determines partial occupations for each wavefunction with a smearing width of 0.12 eV. The Monkhorst-Pack k-point grids [97] are optimized to sample the Brillouin zone with a k-points grid spacing of 0.1 \AA^{-1} . Convergence criteria are set as 10^{-6} eV/atom for total

energy and 10^{-3} eV/\AA for ionic force. Both ground state calculations and *ab initio* molecular dynamics (AIMD) simulation are performed within spin-polarized (collinear) calculations to account for the influence of magnetic moment. More details on the calculation of various properties can be found in the Supplementary Information (SI).

B. Molecular Dynamics Simulations

Molecular dynamics (MD) and static calculations are conducted using the Large-scale Atomic/Molecular Massively Parallel Simulator (LAMMPS) [98]. Atomic structure optimization is performed through the conjugate gradient method, with convergence achieved when forces for all atoms drop below 10^{-10} eV/\AA . For elastic constants, surface energy, grain boundary, stacking fault energy, cohesive and decohesive energies, phonon spectra, and ideal strength, the same box size and configurations are utilized in DFT and MD calculations. A supercell size of $10 \times 10 \times 10$ was employed for MD simulations during the relaxation of self-interstitial defect configurations. More details on methods and settings for the calculations of various properties can be found in the SI.

C. Training Strategy of Deep Potential for Ni

We utilize the general Deep Potential Generator (DP-GEN) scheme [38], the Deep Potential Smooth Edition (DeepPot-SE) [99], in conjunction with the “specialization” strat-

egy [26] to generate the training datasets. We select a fitting neural network size of $240 \times 240 \times 240$ and a cutoff radius of 6 Å. Four models are trained on identical datasets with the same neural network sizes using different random seeds.

Initially, three $2 \times 2 \times 2$ perfect BCC, FCC, and HCP supercells are constructed containing 16, 32, and 16 atoms, respectively. A uniform volume scaling factor (0.96 to 1.06) with a step size of 0.02 is applied, resulting in six configurations for each phase. These scaled configurations are then perturbed three times by introducing random vectors δ of 3% to each of the supercell vectors c_i and 0.01 Å to atom positions R_i , creating distorted supercells. Next, two steps of AIMD simulations are conducted for each distorted structure under the NVT ensemble at 100 K using the Nosé-Hoover thermostat. A total of 108 configurations are obtained from converged ionic steps, providing atomistic information like total energy, atom coordinates R_i , atomic forces f_i , and virial tensors. Spin polarization is considered in DFT calculations for all structures (static and AIMD). This data serves as the initial training datasets to start the DP-GEN loop.

In the training step of the DP-GEN loop, four DP models are initiated by different random seeds. The learning rate starts at 0.001 and exponentially decays to 5×10^{-8} . The training step is set to 400,000. The pre-factors for the energy, atomic force, and virial tensor in the loss functions are assigned as follows: $p_e^{start} = 0.02$, $p_e^{limit} = 2$, $p_f^{start} = 1000$, $p_f^{limit} = 1$, $p_v^{start} = 0$, and $p_v^{limit} = 0$, respectively.

During the exploration step of the DP-GEN loop, a single DP model is selected to explore various bulk and surface structures using DP-based MD (DPMD) with the LAMMPS package. Distorted supercells of $2 \times 2 \times 2$ BCC, FCC, and HCP structures are utilized as starting structures in DPMD. Bulk structure exploration comprises MD simulations in the temperature range of 50 to 3283.2 K (1.9 times the Ni melting point T_{melt}) under an isothermal-isobaric (NPT) ensemble, with pressures varying between 0.001 and 50 kBar. Surface structure exploration commence once all bulk structures have been examined. For surface structures, initial supercells are constructed for low Miller index surfaces, specifically $\{100\}$, $\{110\}$, and $\{111\}$ planes for BCC and FCC structures, and $\{0001\}$ and $\{10\bar{1}0\}$ surfaces for HCP structures. Surface supercells are scaled and perturbed similarly to bulk structures. During the exploration of surface structures, the canonical (NVT) ensemble is employed within the temperature range of 50 to 3283.2 K (1.9 times T_{melt}) for DPMD simulations. The lower and upper bounds of $\sigma\{f_i^\alpha\}$ for exploration are set to 0.10 and 0.25, covering the entire temperature range for both bulk and surface structures. Configurations within $\sigma\{f_i^\alpha\}$ are chosen as candidates and subjected to single-point spin-polarized DFT calculations. The resulting DFT data is then added to the training datasets, generating four new DP models for the subsequent DP-GEN loop. Convergence is achieved when the number of candidate structures for DFT calculation is less than 0.1% of the total number of exploration configurations.

Based on the DP-GEN loop, the final four DP models demonstrate the capability to reproduce the general properties of FCC and HCP Ni. However, the cohesive energy curve

from DP lacks accuracy compared to DFT results. To address this issue, special training datasets are generated, comprising 170 configurations specifically selected from cohesive energy line points. These configurations include 17 distinct structures (spin-polarized calculations are performed), each assigned a weight of 10. Virial tensor and forces are not considered for these new datasets. The ultimate long training is performed on both the training datasets from DP-GEN and “specialization”. The learning rate initiates at 0.001 and exponentially decays to 5×10^{-8} . The training step is 8,000,000 and the pre-factors are $p_e^{start} = 0.02$, $p_e^{limit} = 2$, $p_f^{start} = 1000$, $p_f^{limit} = 1$, $p_v^{start} = 0.02$, and $p_v^{limit} = 1$, respectively. Supplementary Table S2 provides a summary of all the training datasets utilized in this study. It is crucial to highlight that our training dataset is considerably smaller than those reported in other ML potentials [26, 100, 101].

V. DATA AVAILABILITY

The DP-Ni model and the training datasets will be available upon acceptance of the paper.

VI. ACKNOWLEDGMENTS

This work is supported by Research Grants Council, Hong Kong SAR through the Collaborative Research Fund under project number C1005-19G. T.W. acknowledges additional support by The University of Hong Kong (HKU) via seed funds (2201100392, 2309100163). Part of computational resources are supported by research computing facilities offered by Information Technology Services, the University of Hong Kong.

SUPPLEMENTARY INFORMATION

A. Property calculation by DFT

The stress-strain method [102, 103] is applied to evaluate the elastic constants of FCC and HCP Ni. The final values of C_{ij} are obtained by averaging the data after applying a set of normal strain (-0.01, -0.005, 0.005, 0.01) and shear strain (-0.01, -0.005, 0.005, 0.01). The formation energy of mono-vacancy and self-interstitials in FCC Ni are estimated using a $3 \times 3 \times 3$ supercell through full relaxation. Generalized stacking fault γ -lines for the FCC $\{111\}$ planes are calculated using the slab-vacuum supercell method [104]. The atoms are allowed to relax only in the direction perpendicular to the slip plane. These supercells consist of 24 atomic layers and feature a vacuum layer thickness of 20 Å. The slip plane is selected at the center of the supercell. Surface energy and grain boundary energy calculations are performed using configurations with a 20 Å vacuum layer. For $\Sigma 7$ $[111]$ ($3\bar{2}\bar{1}$) configuration, a k-points grid spacing of 0.15 \AA^{-1} is utilized, while other calculation parameters are consistent with the DFT settings in the main text.

The ideal strength of FCC Ni at 0 K is calculated using DFT through the method of incremental loading. The tensile and pure shear strengths along the high symmetry crystallographic directions are identified as the maxima of stress along the incremental loading path simulated by subjecting a suitably oriented periodic supercell of FCC Ni to a combined stress/strain loading, so as to maintain the desired state of stress in the material. In the case of tensile strength determination along a crystallographic direction, at each step of incremental loading, the strain along the tensile axis is held constant (fixed cell vector in that direction), while relaxing all other components of stresses, maintaining a uniaxial state of stress in the material. For FCC crystal, the tensile strengths are determined along the high symmetry directions $[001]$, $[011]$ and $[111]$. The shear strength along a direction on a crystallographic plane is determined by applying a shear strain along that direction and relaxing all other components of stresses thereby achieving the state of pure shear stress in the material. The shear strengths are determined on the (111) plane along the symmetric $[\bar{1}10]$ and $[1\bar{1}0]$ directions, and on the (111) plane along the asymmetric $[11\bar{2}]$ (easy) and $[\bar{1}\bar{1}\bar{2}]$ (hard) directions. The ideal strength under hydrostatic dilatation called tensibility is defined as the maximum hydrostatic stress that the crystal can be subjected to and is determined by incrementally dilating (isotropically expanding) the FCC crystal and at each volume along the loading path, evaluating the resultant hydrostatic stress (negative pressure). The maximum hydrostatic stress along the loading path is the tensibility. Constrained relaxations under combined stress and strain boundary conditions for the ideal strength calculations are achieved through an in-house developed patch to the standard VASP code. In this algorithm, the cell vectors and cell shape, barring those fixed by applied strain boundary conditions and the ionic positions are iteratively optimized until the stress boundary conditions are satisfied.

B. Property calculation by MD

The phonon spectra calculations are performed using PHONOPY [120] and phono-LAMMPS [121] software packages. A $3 \times 3 \times 3$ supercell is applied for the FCC structure, and a $4 \times 4 \times 4$ supercell is employed for the HCP structure.

Lattice parameters and elastic constants at finite temperatures are determined by using a time-averaging approach on individual properties, employing the Nosé-Hoover thermostat in LAMMPS. A fully periodic $16 \text{ nm} \times 16 \text{ nm} \times 16 \text{ nm}$ supercell is initially constructed for a perfect crystal. This supercell is then equilibrated for 40,000 time steps (equivalent to 40,000 fs) under stress-free conditions and at the respective temperatures using MD simulations with an NPT ensemble. After equilibration, the simulation box size is determined by time averaging over 4,000 fs using the same NPT ensemble. The lattice parameter is calculated by dividing the simulation box size by the number of repeating units, and the reported lattice parameters represent the average value obtained from 10 measurements. Elastic constants are also obtained through a time-averaging scheme. The same supercell is subjected to equilibration for 168,000 time steps under stress-free conditions at the target temperatures using an NPT ensemble. An additional 168,000 time steps are performed under the canonical NVT ensemble, applying a $\pm 1\%$ strain in one of the strain components. The stress is measured by averaging the instantaneous stress values obtained at alternate time steps over a period of 14,000 time steps, under the same NVT ensemble. The elastic constants are determined by dividing the mean value of the stress obtained from four measurements by the applied strains. For all interatomic potentials, three repetitions of the calculations are performed, and the average value is considered as the final finite temperature elastic constants.

In this study, we examine the characteristics of $a/2 \langle 110 \rangle$ edge and screw dislocation cores located on the $\{111\}$ plane using a periodic array configuration of dislocations. The slip plane is situated in the x - y plane, perpendicular to the z direction. Periodic boundary conditions are implemented in the x and y directions, while the top and bottom z surfaces are treated as traction-controlled/free surfaces. For the pure edge and screw dislocations, the Burgers vector \mathbf{b} is aligned with the x direction. To reduce the interaction between adjacent dislocation cores, we create sufficiently large supercells. A supercell size of $301 \times 17 \times 85 \text{ \AA}^3$ is used for edge dislocations, and a size of $15 \times 302 \times 85 \text{ \AA}^3$ is used for screw dislocations. For edge dislocation, the dislocation line is along the y direction, namely the dimension of 17 Å, while Burgers vector parallels the x direction, namely the dimension of 301 Å. For the case of screw dislocation, the dislocation line and Burgers vector parallel the x direction, namely the dimension of 15 Å. To introduce the initial full dislocation, we apply the displacement field of the corresponding Volterra dislocation at the center of the supercells by atomsk [122]. Dislocations with a nonzero screw component undergo a homogeneous shear strain of $\epsilon_{yx} = \mathbf{b} \cdot \boldsymbol{\xi}/2$ to rectify the plastic shear strain induced by the screw component. The constructed dislocation cores are subsequently optimized using the conjugate gradient algorithm, with a force convergence criterion set

TABLE S1. Lattice parameters (a), bulk energies (E), cohesive energies (E^{coh}), and elastic constants (C_{ij}) of FCC and HCP Ni by different interatomic potentials. Bold numbers indicate deviations of more than 15% compared to DFT and experiment.

Potential	FCC						HCP								
	a	E	E^{coh}	C_{11}	C_{12}	C_{44}	a	c/a	E	E^{coh}	C_{11}	C_{12}	C_{13}	C_{33}	C_{44}
Expt.	3.520 ^a	-	4.450 ^b	261.2 ^c	150.8 ^c	131.7 ^c	2.487 ^d	1.645 ^d	-	-	-	-	-	-	-
DFT	3.517	-5.467	4.875	275.7	156.0	130.7	2.484	1.643	-5.443	4.851	312.0	142.3	122.8	330.7	55.5
EAM															
Mishin[39]	3.520	-4.450	4.450	247.9	147.8	124.8	2.483	1.619	-4.430	4.430	302.2	147.6	76.9	213.3	64.3
Zhou[105]	3.520	-4.450	4.450	247.0	147.3	124.8	2.483	1.658	-4.434	4.434	302.6	138.1	77.3	247.7	55.6
Foiles[106]	3.520	-4.450	4.450	233.3	154.3	127.6	2.489	1.630	-4.448	4.448	295.7	150.0	95.9	349.6	69.4
Ackland[107]	3.524	-4.459	4.459	260.7	150.5	131.4	2.490	1.642	-4.455	4.455	325.0	141.9	96.9	318.9	77.2
Adams[108]	3.520	-4.450	4.450	235.6	153.1	133.5	2.489	1.630	-4.447	4.447	300.9	148.7	91.9	357.3	72.5
Mendelev[109]	3.518	-4.390	4.390	247.0	147.3	122.8	2.486	1.658	-4.353	4.353	267.0	134.2	58.0	196.7	39.0
Stoller[110]	3.520	-4.450	4.450	240.9	150.5	127.1	2.482	1.654	-4.428	4.428	298.5	145.2	71.6	260.5	48.6
Angelo[111]	3.520	-4.450	4.450	246.5	147.2	125.5	2.480	1.685	-4.437	4.437	276.7	143.5	91.5	257.7	75.3
MEAM															
Etesami[112]	3.520	-4.450	4.450	255.3	155.8	129.8	2.486	1.640	-4.441	4.441	315.8	155.1	97.0	366.2	59.7
Vita[40]	3.519	-3.952	3.952	278.3	169.8	112.5	2.490	1.630	-3.956	3.956	327.6	159.5	131.9	355.6	73.0
Asadi[113]	3.521	-4.450	4.450	260.4	150.7	131.0	2.487	1.641	-4.439	4.439	326.8	139.3	95.9	364.8	74.6
Aitken[114]	3.504	-4.850	4.850	264.2	149.6	125.6	2.471	1.653	-4.825	4.825	331.4	134.7	94.4	358.2	85.4
Shim[115]	3.521	-4.450	4.450	261.2	150.8	131.7	2.484	1.647	-4.429	4.429	332.7	139.0	91.9	366.5	75.0
Shim[116]	3.521	-4.450	4.450	261.2	150.8	131.7	2.484	1.647	-4.429	4.429	332.7	139.0	91.9	366.5	75.0
Ko[41]	3.521	-4.450	4.450	260.4	148.6	111.1	2.487	1.642	-4.440	4.440	314.7	133.8	108.3	336.0	77.2
Maisel[117]	3.521	-4.450	4.450	260.4	148.6	111.1	2.593	1.662	-4.947	4.947	203.8	145.8	133.7	417.5	68.9
Lee[118]	3.521	-4.450	4.450	261.2	150.8	131.7	2.484	1.647	-4.429	4.429	332.7	139.0	91.9	366.5	75.0
Mahata[119]	3.521	-4.450	4.450	260.4	150.7	131.0	2.487	1.641	-4.439	4.439	326.7	139.3	95.9	364.7	74.6
ML(SNAP)															
Zuo[27]	3.521	-5.780	5.780	267.5	155.3	125.7	2.491	1.643	-5.772	5.772	334.0	144.0	109.1	369.2	77.2
Zuo[27]	3.522	-5.781	5.781	282.9	168.3	129.3	2.492	1.650	-5.773	5.773	341.8	166.9	132.5	421.0	63.6

^a [42]

^b [43]

^c [44]

^d [46]

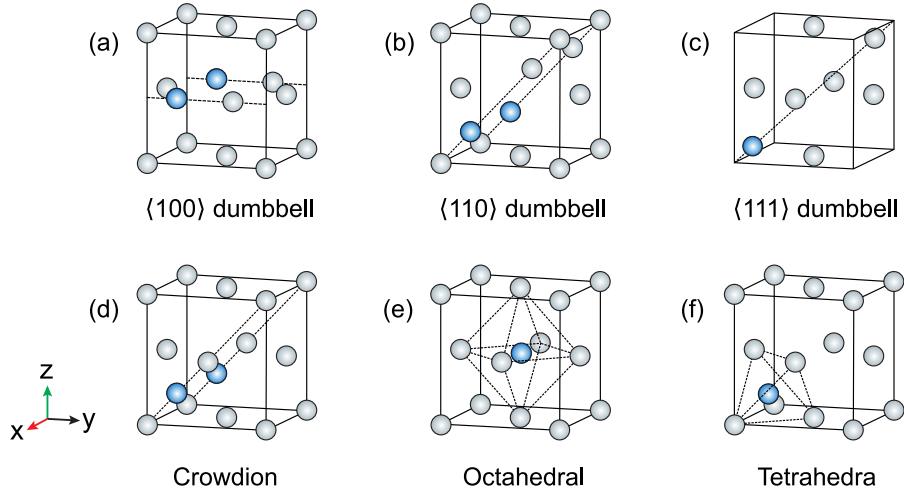


FIG. S1. Six types of self-interstitial configurations in the FCC crystal lattice.

to 10^{-4} eV/Å. The final atomic configurations are visualized through the open visualization tool (OVITO) [66]. Additionally, differential displacement plots are analyzed utilizing the

atomistic manipulation toolkit atomman [123].

TABLE S2. Summary of the training datasets for DP Ni.

Dataset type	Number of datasets	Weightage
Initialization datasets	108	1
DP-GEN bulk	1140	1
DP-GEN surface	602	1
Cohesive energy	17	10
Total ^a	2020	

^a The cohesive energy datasets are considered as $17 \times 10 = 170$.

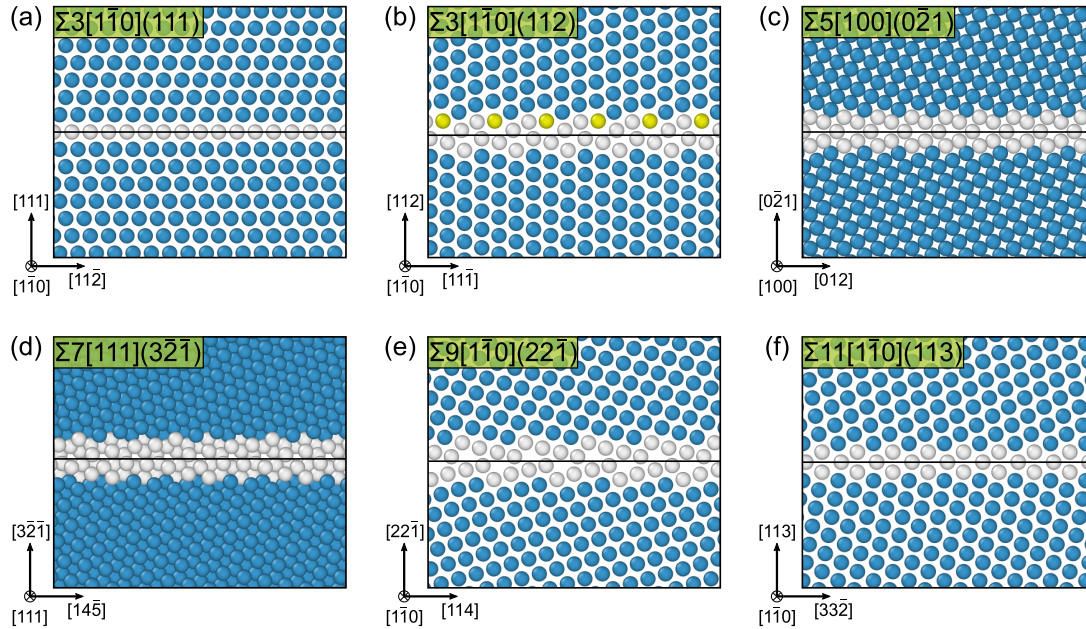


FIG. S2. The optimized tilt grain boundary structures in FCC Ni using DP-Ni. The relaxed (a) $\Sigma 3 [1\bar{1}0] (111)$, (c) $\Sigma 5 [100] (0\bar{2}1)$ and (f) $\Sigma 11 [1\bar{1}0] (113)$ yield twinning configurations, while (b) $\Sigma 3 [1\bar{1}0] (112)$, (d) $\Sigma 7 [111] (3\bar{2}1)$ and (e) $\Sigma 9 [1\bar{1}0] (2\bar{2}1)$ are asymmetric boundary structures. The atomic configurations are visualized using the open visualization tool (OVITO) [66] with the application of the common neighbor analysis (CNA) method [67]. The FCC, HCP and other types of atoms are marked in blue, yellow and white, respectively.

REFERENCES

- [1] D. C. Adriano, Nickel, in *Trace Elements in Terrestrial Environments: Biogeochemistry, Bioavailability, and Risks of Metals* (Springer New York, New York, NY, 2001) pp. 677–705.
- [2] W. Mankins and S. Lamb, Nickel and nickel alloys, in *Properties and Selection: Nonferrous Alloys and Special-Purpose Materials* (ASM International, 1990).
- [3] J. Everhart, *Engineering properties of nickel and nickel alloys* (Springer Science & Business Media, 2012).
- [4] M. B. Henderson, D. Arrell, R. Larsson, M. Heobel, and G. Marchant, Nickel based superalloy welding practices for industrial gas turbine applications, *Science and Technology of Welding and Joining* **9**, 13 (2004).
- [5] R. Darolia, Development of strong, oxidation and corrosion resistant nickel-based superalloys: critical review of challenges, progress and prospects, *International Materials Reviews* **64**, 355 (2019).
- [6] A. Sato, Y.-L. Chiu, and R. Reed, Oxidation of nickel-based single-crystal superalloys for industrial gas turbine applications, *Acta Materialia* **59**, 225 (2011).
- [7] A. Shukla, S. Venugopalan, and B. Hariprakash, Nickel-based rechargeable batteries, *Journal of Power Sources* **100**, 125 (2001).
- [8] W. Keim, Nickel: An element with wide application in industrial homogeneous catalysis, *Angewandte Chemie International Edition in English* **29**, 235 (1990).
- [9] D. L. Trimm, The formation and removal of coke from nickel catalyst, *Catalysis Reviews* **16**, 155 (1977).
- [10] E. P. George, D. Raabe, and R. O. Ritchie, High-entropy alloys, *Nature Reviews Materials* **4**, 515 (2019).
- [11] B. Gludovatz, A. Hohenwarther, K. V. Thurston, H. Bei, Z. Wu, E. P. George, and R. O. Ritchie, Exceptional damage-tolerance of a medium-entropy alloy CrCoNi at cryogenic temperatures, *Nature Communications* **7**, 10602 (2016).
- [12] X. Xu, X. Zhang, A. Ruban, S. Schmauder, and B. Grabowski, Strong impact of spin fluctuations on the antiphase boundaries of weak itinerant ferromagnetic Ni₃Al, *Acta Materialia* **255**, 118986 (2023).
- [13] V. Borovikov, M. I. Mendeleev, A. H. King, and R. LeSar, Effect of stacking fault energy on mechanism of plastic deformation in nanotwinned fcc metals, *Modelling and Simulation in Materials Science and Engineering* **23**, 055003 (2015).
- [14] Y. Mishin, Machine-learning interatomic potentials for materials science, *Acta Materialia* **214**, 116980 (2021).

- [15] J. Tersoff, Empirical interatomic potential for carbon, with applications to amorphous carbon, *Physical Review Letters* **61**, 2879 (1988).
- [16] M.-C. Marinica, L. Ventelon, M. R. Gilbert, L. Proville, S. L. Dudarev, J. Marian, G. Bencteux, and F. Willaime, Interatomic potentials for modelling radiation defects and dislocations in tungsten, *Journal of Physics: Condensed Matter* **25**, 395502 (2013).
- [17] Interatomic potentials repository: <https://www.ctcms.nist.gov/potentials/system/Ni/>.
- [18] Open knowledgebase of interatomic models: <https://openkim.org/browse/models/by-species?species-search=Ni>.
- [19] A. S. Pattamatta and D. J. Srolovitz, Allotropy in ultra high strength materials, *Nature Communications* **13**, 3326 (2022).
- [20] A. Krygier, P. D. Powell, J. M. McNaney, C. M. Huntington, S. T. Prisbrey, B. A. Remington, R. E. Rudd, D. C. Swift, C. E. Wehrenberg, A. Arsenlis, H.-S. Park, P. Graham, E. Gumbrell, M. P. Hill, A. J. Comley, and S. D. Rothman, Extreme hardening of Pb at high pressure and strain rate, *Physical Review Letters* **123**, 205701 (2019).
- [21] Z. Luo, X. Guo, J. Hou, X. Zhou, X. Li, and K. Lu, Plastic deformation induced hexagonal-close-packed nickel nano-grains, *Scripta Materialia* **168**, 67 (2019).
- [22] Q. Yu, J. Kacher, C. Gammer, R. Traylor, A. Samanta, Z. Yang, and A. M. Minor, In situ TEM observation of FCC Ti formation at elevated temperatures, *Scripta Materialia* **140**, 9 (2017).
- [23] X. Guo, Z. Luo, X. Li, and K. Lu, Plastic deformation induced extremely fine nano-grains in nickel, *Materials Science and Engineering: A* **802**, 140664 (2021).
- [24] W. Tian, H. P. Sun, X. Q. Pan, J. H. Yu, M. Yeadon, C. B. Boothroyd, Y. P. Feng, R. A. Lukaszew, and R. Clarke, Hexagonal close-packed Ni nanostructures grown on the (001) surface of MgO, *Applied Physics Letters* **86**, 131915 (2005).
- [25] J. Higuchi, M. Ohtake, Y. Sato, T. Nishiyama, and M. Futamoto, Preparation and structural characterization of hcp and fcc ni epitaxial thin films on ru underlayers with different orientations, *Japanese Journal of Applied Physics* **50**, 063001 (2011).
- [26] T. Wen, R. Wang, L. Zhu, L. Zhang, H. Wang, D. J. Srolovitz, and Z. Wu, Specialising neural network potentials for accurate properties and application to the mechanical response of titanium, *npj Computational Materials* **7**, 206 (2021).
- [27] Y. Zuo, C. Chen, X. Li, Z. Deng, Y. Chen, J. Behler, G. Csányi, A. V. Shapeev, A. P. Thompson, M. A. Wood, and S. P. Ong, Performance and cost assessment of machine learning interatomic potentials, *The Journal of Physical Chemistry A* **124**, 731 (2020), pMID: 31916773.
- [28] X.-G. Li, C. Hu, C. Chen, Z. Deng, J. Luo, and S. P. Ong, Quantum-accurate spectral neighbor analysis potential models for Ni-Mo binary alloys and fcc metals, *Physical Review B* **98**, 094104 (2018).
- [29] M.-T. Suzuki, T. Nomoto, E. V. Morooka, Y. Yanagi, and H. Kusunose, High-performance descriptor for magnetic materials: Accurate discrimination of magnetic structure, *Physical Review B* **108**, 014403 (2023).
- [30] I. Novikov, B. Grabowski, F. Körmann, and A. Shapeev, Magnetic Moment Tensor Potentials for collinear spin-polarized materials reproduce different magnetic states of bcc Fe, *npj Computational Materials* **8**, 13 (2022).
- [31] H. Yu, Y. Zhong, J. Ji, X. Gong, and H. Xiang, Time-reversal equivariant neural network potential and Hamiltonian for magnetic materials, arXiv preprint arXiv:2211.11403 (2022).
- [32] P. Zhang and G.-W. Chern, Machine learning nonequilibrium electron forces for spin dynamics of itinerant magnets, *npj Computational Materials* **9**, 32 (2023).
- [33] A. Egorov, A. P. A. Subramanyam, Z. Yuan, R. Drautz, and T. Hammerschmidt, Magnetic bond-order potential for iron-cobalt alloys, *Physical Review Materials* **7**, 044403 (2023).
- [34] I. Toda-Caraballo, J. S. Wróbel, and D. Nguyen-Manh, Generalized universal equation of states for magnetic materials: A novel formulation for an interatomic potential in Fe, *Physical Review Materials* **6**, 043806 (2022).
- [35] J. B. Chapman and P.-W. Ma, A machine-learned spin-lattice potential for dynamic simulations of defective magnetic iron, *Scientific Reports* **12**, 22451 (2022).
- [36] H. Yu, Y. Zhong, L. Hong, C. Xu, W. Ren, X. Gong, and H. Xiang, Spin-dependent graph neural network potential for magnetic materials, arXiv preprint arXiv:2203.02853 10.48550/arXiv.2203.02853 (2022).
- [37] T. Wen, L. Zhang, H. Wang, W. E, and D. J. Srolovitz, Deep potentials for materials science, *Materials Futures* **1**, 022601 (2022).
- [38] Y. Zhang, H. Wang, W. Chen, J. Zeng, L. Zhang, H. Wang, and W. E, DP-GEN: A concurrent learning platform for the generation of reliable deep learning based potential energy models, *Computer Physics Communications* **253**, 107206 (2020).
- [39] Y. Mishin, D. Farkas, M. J. Mehl, and D. A. Papaconstantopoulos, Interatomic potentials for monoatomic metals from experimental data and ab initio calculations, *Physical Review B* **59**, 3393 (1999).
- [40] J. A. Vita and D. R. Trinkle, Exploring the necessary complexity of interatomic potentials, *Computational Materials Science* **200**, 110752 (2021).
- [41] W.-S. Ko, B. Grabowski, and J. Neugebauer, Development and application of a Ni-Ti interatomic potential with high predictive accuracy of the martensitic phase transition, *Physical Review B* **92**, 134107 (2015).
- [42] N. S. Kanhe, A. Kumar, S. Yusuf, A. Nawale, S. Gaikwad, S. A. Raut, S. Bhoraskar, S. Y. Wu, A. Das, and V. Mathe, Investigation of structural and magnetic properties of thermal plasma-synthesized $\text{Fe}_{1-x}\text{Ni}_x$ alloy nanoparticles, *Journal of Alloys and Compounds* **663**, 30 (2016).
- [43] C. Kittel, *Introduction to solid state physics* (John Wiley & sons, inc, 2005).
- [44] G. Simmons and H. Wang, Single crystal elastic constants and calculated aggregate properties: a handbook, The MIT Press (1971).
- [45] A. Dinsdale, SGTE data for pure elements, *Calphad* **15**, 317 (1991).
- [46] A. P. LaGrow, S. Cheong, J. Watt, B. Ingham, M. F. Toney, D. A. Jefferson, and R. D. Tilley, Can polymorphism be used to form branched metal nanostructures?, *Advanced Materials* **25**, 1552 (2013).
- [47] M. Born, Thermodynamics of crystals and melting, *The Journal of Chemical Physics* **7**, 591 (2004).
- [48] R. Birgeneau, J. Cordes, G. Dolling, and A. D. B. Woods, Normal modes of vibration in nickel, *Physical Review* **136**, A1359 (1964).
- [49] G. Grimvall, B. Magyari-Köpe, V. Ozoliņš, and K. A. Persson, Lattice instabilities in metallic elements, *Reviews of Modern Physics* **84**, 945 (2012).
- [50] W. Tyson and W. Miller, Surface free energies of solid metals: Estimation from liquid surface tension measurements, *Surface Science* **62**, 267 (1977).
- [51] E. H. Megchiche, S. Pérusin, J.-C. Barthelat, and C. Mijoule,

- Density functional calculations of the formation and migration enthalpies of monovacancies in Ni: Comparison of local and nonlocal approaches, *Physical Review B* **74**, 064111 (2006).
- [52] C. B. Carter and S. M. Holmes, The stacking-fault energy of nickel, *The Philosophical Magazine: A Journal of Theoretical Experimental and Applied Physics* **35**, 1161 (1977).
- [53] L. E. Murr, *Interfacial phenomena in metals and alloys* (1975).
- [54] R. Tran, Z. Xu, B. Radhakrishnan, D. Winston, W. Sun, K. A. Persson, and S. P. Ong, Surface energies of elemental crystals, *Scientific data* **3**, 1 (2016).
- [55] E. Toijer, L. Messina, C. Domain, J. Vidal, C. Becquart, and P. Olsson, Solute-point defect interactions, coupled diffusion, and radiation-induced segregation in fcc nickel, *Physical Review Materials* **5**, 013602 (2021).
- [56] J. Tucker, T. Allen, R. Najafabadi, T. Allen, and D. Morgan, Determination of solute-interstitial interactions in Ni-Cr by first principle, in *Int. Conf. Adv. Math. Comput. Methods React. Physics, MC*, Vol. 2 (2009) p. 891.
- [57] P.-W. Ma and S. Dudarev, Nonuniversal structure of point defects in face-centered cubic metals, *Physical Review Materials* **5**, 013601 (2021).
- [58] S.-H. Jhi, S. G. Louie, M. L. Cohen, and J. Morris Jr, Mechanical instability and ideal shear strength of transition metal carbides and nitrides, *Physical Review Letters* **87**, 075503 (2001).
- [59] I.-K. Suh, H. Ohta, and Y. Waseda, High-temperature thermal expansion of six metallic elements measured by dilatation method and X-ray diffraction, *Journal of Materials Science* **23**, 757 (1988).
- [60] G. Hachet, A. Metsue, A. Oudriss, and X. Feugas, Influence of hydrogen on the elastic properties of nickel single crystal: A numerical and experimental investigation, *Acta Materialia* **148**, 280 (2018).
- [61] G. Alers, J. Neighbours, and H. Sato, Temperature dependent magnetic contributions to the high field elastic constants of nickel and an Fe-Ni alloy, *Journal of Physics and Chemistry of Solids* **13**, 40 (1960).
- [62] J. Xiao, L. Zhu, R. Wang, C. Deng, Z. Wu, and Y. Zhu, Unveiling deformation twin nucleation and growth mechanisms in BCC transition metals and alloys, *Materials Today* **65**, 90 (2023).
- [63] J. W. Christian and V. Vitek, Dislocations and stacking faults, *Reports on Progress in Physics* **33**, 307 (1970).
- [64] Y. Su, S. Xu, and I. J. Beyerlein, Density functional theory calculations of generalized stacking fault energy surfaces for eight face-centered cubic transition metals, *Journal of Applied Physics* **126**, 105112 (2019).
- [65] D. Rodney, L. Ventelon, E. Clouet, L. Pizzagalli, and F. Willaume, Ab initio modeling of dislocation core properties in metals and semiconductors, *Acta Materialia* **124**, 633 (2017).
- [66] A. Stukowski, Visualization and analysis of atomistic simulation data with OVITO—the Open Visualization Tool, *Modelling and Simulation in Materials Science and Engineering* **18**, 015012 (2009).
- [67] J. D. Honeycutt and H. C. Andersen, Molecular dynamics study of melting and freezing of small Lennard-Jones clusters, *Journal of Physical Chemistry* **91**, 4950 (1987).
- [68] A. Stukowski and K. Albe, Extracting dislocations and non-dislocation crystal defects from atomistic simulation data, *Modelling and Simulation in Materials Science and Engineering* **18**, 085001 (2010).
- [69] P. M. Anderson, J. P. Hirth, and J. Lothe, *Theory of dislocations* (Cambridge University Press, 2017).
- [70] V. Vitek, R. C. Perrin, and D. K. Bowen, The core structure of $\frac{1}{2}(111)$ screw dislocations in b.c.c. crystals, *The Philosophical Magazine: A Journal of Theoretical Experimental and Applied Physics* **21**, 1049 (1970).
- [71] A. M. Z. Tan, C. Woodward, and D. R. Trinkle, Dislocation core structures in Ni-based superalloys computed using a density functional theory based flexible boundary condition approach, *Physical Review Materials* **3**, 033609 (2019).
- [72] V. Randle and G. Owen, Mechanisms of grain boundary engineering, *Acta Materialia* **54**, 1777 (2006).
- [73] Q. Zhu, G. Cao, J. Wang, C. Deng, J. Li, Z. Zhang, and S. X. Mao, In situ atomistic observation of disconnection-mediated grain boundary migration, *Nature communications* **10**, 156 (2019).
- [74] H. Khater, A. Serra, R. Pond, and J. Hirth, The disconnection mechanism of coupled migration and shear at grain boundaries, *Acta Materialia* **60**, 2007 (2012).
- [75] N. Lu, K. Du, L. Lu, and H. Ye, Transition of dislocation nucleation induced by local stress concentration in nanotwinned copper, *Nature communications* **6**, 7648 (2015).
- [76] P. Chen, F. Wang, and B. Li, Transitory phase transformations during $\{10\bar{1}2\}$ twinning in titanium, *Acta Materialia* **171**, 65 (2019).
- [77] X. Guan, Q. Chen, S. Qu, G. Cao, H. Wang, X. Ran, A. Feng, and D. Chen, High-strain-rate deformation: Stress-induced phase transformation and nanostructures in a titanium alloy, *International Journal of Plasticity* **169**, 103707 (2023).
- [78] S. Li, Z. Jin, X. Gong, H. Huang, S. Guan, and G. Yuan, Chemical ordering effects on martensitic transformations in Mg-Sc alloys, *Acta Materialia* **249**, 118854 (2023).
- [79] X.-S. Yang, S. Sun, H.-H. Ruan, S.-Q. Shi, and T.-Y. Zhang, Shear and shuffling accomplishing polymorphic fcc $\gamma \rightarrow$ hcp $\varepsilon \rightarrow$ bct α martensitic phase transformation, *Acta Materialia* **136**, 347 (2017).
- [80] J. Hirth, R. Hoagland, B. Holian, and T. Germann, Shock relaxation by a strain induced martensitic phase transformation, *Acta Materialia* **47**, 2409 (1999).
- [81] S. Sun, D. Li, C. Yang, L. Fu, D. Kong, Y. Lu, Y. Guo, D. Liu, P. Guan, Z. Zhang, J. Chen, W. Ming, L. Wang, and X. Han, Direct atomic-scale observation of ultrasmall Ag nanowires that exhibit fcc, bcc, and hcp structures under bending, *Physical Review Letters* **128**, 015701 (2022).
- [82] H. Xie, F. Yin, T. Yu, G. Lu, and Y. Zhang, A new strain-rate-induced deformation mechanism of Cu nanowire: Transition from dislocation nucleation to phase transformation, *Acta Materialia* **85**, 191 (2015).
- [83] S. Wei, J. Kim, J. L. Cann, R. Gholizadeh, N. Tsuji, and C. C. Tasan, Plastic strain-induced sequential martensitic transformation, *Scripta Materialia* **185**, 36 (2020).
- [84] H. Zhang, X. Huang, and N. Hansen, Evolution of microstructural parameters and flow stresses toward limits in nickel deformed to ultra-high strains, *Acta Materialia* **56**, 5451 (2008).
- [85] A. Krygier, P. D. Powell, J. M. McNaney, C. M. Huntington, S. T. Prisbrey, B. A. Remington, R. E. Rudd, D. C. Swift, C. E. Wehrenberg, A. Arsenlis, H.-S. Park, P. Graham, E. Gumbrell, M. P. Hill, A. J. Comley, and S. D. Rothman, Extreme hardening of Pb at high pressure and strain rate, *Physical Review Letters* **123**, 205701 (2019).
- [86] S. Li, N. Chen, A. Rohatgi, Y. Li, C. A. Powell, S. Mathaudhu, A. Devaraj, S. Hu, and C. Wang, Nanotwin assisted reversible formation of low angle grain boundary upon reciprocating shear load, *Acta Materialia* **230**, 117850 (2022).
- [87] J. Diao, K. Gall, and M. L. Dunn, Surface-stress-induced phase transformation in metal nanowires, *Nature Materials* **2**,

- 656 (2003).
- [88] T. Wu, M. Sun, H. H. Wong, and B. Huang, Decoding of crystal synthesis of fcc-hcp reversible transition for metals: theoretical mechanistic study from facet control to phase transition engineering, *Nano Energy* **85**, 106026 (2021).
- [89] R. M. Wentzcovitch and P. K. Lam, fcc-to-hcp transformation: A first-principles investigation, *Physical Review B* **44**, 9155 (1991).
- [90] F. Bai, Q. Zhu, J. Shen, Z. Lu, L. Zhang, N. Ali, H. Zhou, and X. Liu, Study on phase transformation orientation relationship of hcp-fcc during rolling of high purity titanium, *Crystals* **11**, 1164 (2021).
- [91] D. Zhang, H. Bi, F.-Z. Dai, W. Jiang, L. Zhang, and H. Wang, DPA-1: Pretraining of attention-based Deep Potential Model for molecular simulation (2022), [arXiv:2208.08236 \[physics.chem-ph\]](https://arxiv.org/abs/2208.08236).
- [92] G. Kresse and J. Furthmüller, Efficiency of ab-initio total energy calculations for metals and semiconductors using a plane-wave basis set, *Computational Materials Science* **6**, 15 (1996).
- [93] G. Kresse and J. Furthmüller, Efficient iterative schemes for ab initio total-energy calculations using a plane-wave basis set, *Physical Review B* **54**, 11169 (1996).
- [94] P. E. Blöchl, Projector augmented-wave method, *Physical Review B* **50**, 17953 (1994).
- [95] J. P. Perdew, K. Burke, and M. Ernzerhof, Generalized gradient approximation made simple, *Physical Review Letters* **77**, 3865 (1996).
- [96] M. Methfessel and A. Paxton, High-precision sampling for Brillouin-zone integration in metals, *Physical Review B* **40**, 3616 (1989).
- [97] H. J. Monkhorst and J. D. Pack, Special points for Brillouin-zone integrations, *Physical Review B* **13**, 5188 (1976).
- [98] A. P. Thompson, H. M. Aktulga, R. Berger, D. S. Bolintineanu, W. M. Brown, P. S. Crozier, P. J. in 't Veld, A. Kohlmeyer, S. G. Moore, T. D. Nguyen, R. Shan, M. J. Stevens, J. Tranchida, C. Trott, and S. J. Plimpton, LAMMPS - a flexible simulation tool for particle-based materials modeling at the atomic, meso, and continuum scales, *Computer Physics Communications* **271**, 108171 (2022).
- [99] L. Zhang, J. Han, H. Wang, W. Saidi, R. Car, and W. E, End-to-end symmetry preserving inter-atomic potential energy model for finite and extended systems, in *Advances in Neural Information Processing Systems*, Vol. 31, edited by S. Bengio, H. Wallach, H. Larochelle, K. Grauman, N. Cesa-Bianchi, and R. Garnett (Curran Associates, Inc., 2018).
- [100] J. Byggmästar, K. Nordlund, and F. Djurabekova, Gaussian approximation potentials for body-centered-cubic transition metals, *Physical Review Materials* **4**, 093802 (2020).
- [101] J. S. Smith, B. Nebgen, N. Mathew, J. Chen, N. Lubbers, L. Burakovsky, S. Tretyak, H. A. Nam, T. Germann, S. Fensin, *et al.*, Automated discovery of a robust interatomic potential for aluminum, *Nature communications* **12**, 1257 (2021).
- [102] S. Shang, Y. Wang, and Z.-K. Liu, First-principles elastic constants of α - and θ -Al₂O₃, *Applied Physics Letters* **90**, 101909 (2007).
- [103] X. Gong, W.-W. Xu, C. Cui, Q. Yu, W. Wang, T. Gang, and L. Chen, Exploring alloying effect on phase stability and mechanical properties of γ' -Ni₃Nb precipitates with first-principles calculations, *Materials & Design* **196**, 109174 (2020).
- [104] V. Vitek, Intrinsic stacking faults in body-centred cubic crystals, *The Philosophical Magazine: A Journal of Theoretical Experimental and Applied Physics* **18**, 773 (1968).
- [105] X. Zhou, R. Johnson, and H. Wadley, Misfit-energy-increasing dislocations in vapor-deposited CoFe/NiFe multilayers, *Physical Review B* **69**, 144113 (2004).
- [106] S. Foiles, M. Baskes, and M. S. Daw, Embedded-atom-method functions for the fcc metals Cu, Ag, Au, Ni, Pd, Pt, and their alloys, *Physical review B* **33**, 7983 (1986).
- [107] G. J. Ackland, G. Tichy, V. Vitek, and M. W. Finnis, Simple N-body potentials for the noble metals and nickel, *Philosophical Magazine A* **56**, 735 (1987).
- [108] J. Adams, S. Foiles, and W. Wolfer, Self-diffusion and impurity diffusion of fee metals using the five-frequency model and the embedded atom method, *Journal of Materials Research* **4**, 102 (1989).
- [109] M. Mendeleev, M. Kramer, S. Hao, K. Ho, and C. Wang, Development of interatomic potentials appropriate for simulation of liquid and glass properties of NiZr₂ alloy, *Philosophical Magazine* **92**, 4454 (2012).
- [110] R. Stoller, A. Tamm, L. Béland, G. Samolyuk, G. Stocks, A. Caro, L. Slipchenko, Y. N. Osetsky, A. Aabloo, M. Klintonberg, *et al.*, Impact of short-range forces on defect production from high-energy collisions, *Journal of Chemical Theory and Computation* **12**, 2871 (2016).
- [111] J. E. Angelo, N. R. Moody, and M. I. Baskes, Trapping of hydrogen to lattice defects in nickel, *Modelling and Simulation in Materials Science and Engineering* **3**, 289 (1995).
- [112] S. A. Etesami and E. Asadi, Molecular dynamics for near melting temperatures simulations of metals using modified embedded-atom method, *Journal of Physics and Chemistry of Solids* **112**, 61 (2018).
- [113] E. Asadi, M. Asle Zaeem, S. Nouranian, and M. I. Baskes, Two-phase solid-liquid coexistence of Ni, Cu, and Al by molecular dynamics simulations using the modified embedded-atom method, *Acta Materialia* **86**, 169 (2015).
- [114] Z. H. Aitken, V. Sorokin, Z. G. Yu, S. Chen, Z. Wu, and Y.-W. Zhang, Modified embedded-atom method potentials for the plasticity and fracture behaviors of unary fcc metals, *Physical Review B* **103**, 094116 (2021).
- [115] J.-H. Shim, S. I. Park, Y. W. Cho, and B.-J. Lee, Modified embedded-atom method calculation for the Ni-W system, *Journal of Materials Research* **18**, 1863 (2003).
- [116] J.-H. Shim, W.-S. Ko, K.-H. Kim, H.-S. Lee, Y.-S. Lee, J.-Y. Suh, Y. W. Cho, and B.-J. Lee, Prediction of hydrogen permeability in V-Al and V-Ni alloys, *Journal of Membrane Science* **430**, 234 (2013).
- [117] S. B. Maisel, W.-S. Ko, J.-L. Zhang, B. Grabowski, and J. Neugebauer, Thermomechanical response of NiTi shape-memory nanoprecipitates in TiV alloys, *Physical Review Materials* **1**, 033610 (2017).
- [118] B.-J. Lee, J.-H. Shim, and M. Baskes, Semiempirical atomic potentials for the fcc metals Cu, Ag, Au, Ni, Pd, Pt, Al, and Pb based on first and second nearest-neighbor modified embedded atom method, *Physical Review B* **68**, 144112 (2003).
- [119] A. Mahata, T. Mukhopadhyay, and M. Asle Zaeem, Modified embedded-atom method interatomic potentials for Al-Cu, Al-Fe and Al-Ni binary alloys: From room temperature to melting point, *Computational Materials Science* **201**, 110902 (2022).
- [120] A. Togo and I. Tanaka, First principles phonon calculations in materials science, *Scripta Materialia* **108**, 1 (2015).
- [121] A. Carreras, phonoLAMMPS: <https://phonolammps.readthedocs.io/en/master/index.html>.
- [122] P. Hirel, Atomsk: A tool for manipulating and converting atomic data files, *Computer Physics Communications* **197**, 212 (2015).
- [123] atomman: Atomistic manipulation toolkit: <https://www.ctcms.nist.gov/potentials/atomman/>.